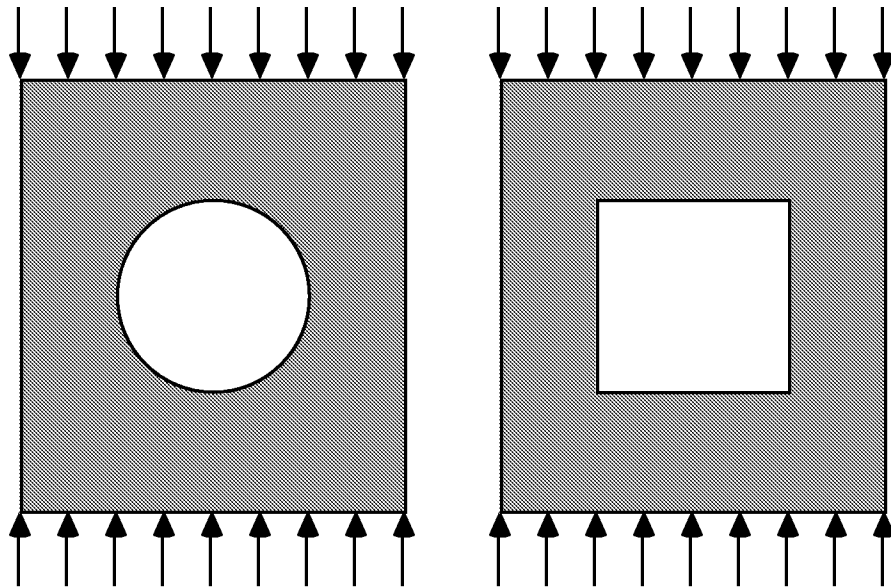


Mechanical- and Thermal-Buckling Behavior of Rectangular Plates With Different Central Cutouts

William L. Ko
Dryden Flight Research Center
Edwards, California



The NASA STI Program Office . . . in Profile

Since its founding, NASA has been dedicated to the advancement of aeronautics and space science. The NASA Scientific and Technical Information (STI) Program Office plays a key part in helping NASA maintain this important role.

The NASA STI Program Office is operated by Langley Research Center, the lead center for NASA's scientific and technical information. The NASA STI Program Office provides access to the NASA STI Database, the largest collection of aeronautical and space science STI in the world. The Program Office is also NASA's institutional mechanism for disseminating the results of its research and development activities. These results are published by NASA in the NASA STI Report Series, which includes the following report types:

- **TECHNICAL PUBLICATION.** Reports of completed research or a major significant phase of research that present the results of NASA programs and include extensive data or theoretical analysis. Includes compilations of significant scientific and technical data and information deemed to be of continuing reference value. NASA's counterpart of peer-reviewed formal professional papers but has less stringent limitations on manuscript length and extent of graphic presentations.
- **TECHNICAL MEMORANDUM.** Scientific and technical findings that are preliminary or of specialized interest, e.g., quick release reports, working papers, and bibliographies that contain minimal annotation. Does not contain extensive analysis.
- **CONTRACTOR REPORT.** Scientific and technical findings by NASA-sponsored contractors and grantees.

- **CONFERENCE PUBLICATION.** Collected papers from scientific and technical conferences, symposia, seminars, or other meetings sponsored or cosponsored by NASA.
- **SPECIAL PUBLICATION.** Scientific, technical, or historical information from NASA programs, projects, and mission, often concerned with subjects having substantial public interest.
- **TECHNICAL TRANSLATION.** English-language translations of foreign scientific and technical material pertinent to NASA's mission.

Specialized services that complement the STI Program Office's diverse offerings include creating custom thesauri, building customized databases, organizing and publishing research results . . . even providing videos.

For more information about the NASA STI Program Office, see the following:

- Access the NASA STI Program Home Page at <http://www.sti.nasa.gov>
- E-mail your question via the Internet to help@sti.nasa.gov
- Fax your question to the NASA Access Help Desk at (301) 621-0134
- Telephone the NASA Access Help Desk at (301) 621-0390
- Write to:
NASA Access Help Desk
NASA Center for Aerospace Information
800 Elkridge Landing Road
Linthicum Heights, MD 21090-2934

NASA/TM-1998-206542



Mechanical- and Thermal-Buckling Behavior of Rectangular Plates With Different Central Cutouts

*William L. Ko
Dryden Flight Research Center
Edwards, California*

National Aeronautics and
Space Administration

Dryden Flight Research Center
Edwards, California 93523-0273

March 1998

NOTICE

Use of trade names or names of manufacturers in this document does not constitute an official endorsement of such products or manufacturers, either expressed or implied, by the National Aeronautics and Space Administration.

Available from:

NASA Center for AeroSpace Information
800 Elkridge Landing Road
Linthicum Heights, MD 21090-2934
Price Code: A16

National Technical Information Service
5285 Port Royal Road
Springfield, VA 22161
Price Code: A16

CONTENTS

	<u>Page</u>
ABSTRACT	1
NOMENCLATURE	1
INTRODUCTION	2
DESCRIPTION OF THE PROBLEM	3
Geometry.....	3
Boundary Conditions	4
Mechanical Buckling	4
Thermal Buckling	4
FINITE-ELEMENT ANALYSIS.....	4
MATERIAL PROPERTY ITERATIONS	6
RESULTS	6
Solution Accuracy.....	6
Plates With Circular Holes	7
Mechanical Buckling for Fixed-Boundary Cases.....	7
Mechanical Buckling for Free-Boundary Cases.....	8
Thermal Buckling	8
Plates With Square Holes	8
Mechanical Buckling for Fixed-Boundary Cases.....	8
Mechanical Buckling for Free-Boundary Cases.....	9
Thermal Buckling	9
Comparison of Buckling Strengths.....	9
DISCUSSION.....	10
CONCLUDING REMARKS	10
REFERENCES	12
FIGURES	13

ABSTRACT

Mechanical- and thermal-buckling analyses were performed on rectangular plates with central cutouts. The cutouts were either circular holes or square holes. The finite-element structural analysis method was used to study the effects of plate-support conditions, plate aspect ratio, hole geometry, and hole size on the mechanical- and thermal-buckling strengths of the perforated plates. By increasing the hole size, thermal-buckling strengths of the plates could be enhanced. The compressive-buckling strengths of the plates could also be increased considerably only under certain boundary conditions and aspect ratios. The plate-buckling mode can be symmetrical or antisymmetrical, depending on the plate boundary conditions, aspect ratio, and the hole size. For the same cutout areas (i.e., same plate weight density), the buckling strengths of the same-sized plates with square holes generally surpass those of the plates with circular holes over the range of hole sizes. The results and illustrations provide vital information for the efficient design of aerospace structural panels.

NOMENCLATURE

c	side of square hole, in.
d	diameter of circular hole, in.
E	Young's modulus, lb/in ²
E33	triangular combined membrane and bending element
E43	quadrilateral combined membrane and bending element
G	shear modulus, lb/in ²
JLOC	joint location (or grid point or node)
l	length of rectangular plates, in.
N_y	compressive force intensity in y-direction, lb/in.
SPAR	structural performance and resizing finite-element computer program
T	temperature, °F
T_a	assumed temperature for material, °F
T_r	room temperature, $T_r = 70$ °F
t	thickness of plates, in.
w	width of plates, in.
x, y	rectangular Cartesian coordinates
α	coefficient of thermal expansion, in/in-°F
ΔT	temperature increase, °F
ν	Poisson's ratio

Subscripts

$()_{cr}$	critical value at buckling
$()_n$	n^{th} iteration ($n = 1, 2, 3 \dots$)

INTRODUCTION

In aerospace structures, cutouts are commonly used as access ports for mechanical and electrical systems, or simply to reduce weight. Structural panels with cutouts often experience compressive loads that are induced either mechanically or thermally, and can result in panel buckling. Thus, the buckling behavior of those structural panels with cutouts must be fully understood in the structural design.

For an unperforated rectangular plate of finite extent (i.e., with finite length and finite width) under uniform compression, the closed-form buckling solutions are easily obtained because the prebuckling stress field is uniform everywhere in the plate. When a finite rectangular plate is perforated with a central cutout (e.g., a circular or square hole), however, the buckling analysis becomes extremely cumbersome because the cutout introduces a load-free boundary that causes the stress field in the perforated plate to be nonuniform. Hence, the closed-form buckling solutions are practically unobtainable, and various approximate methods had to be developed to analyze such perforated plates.

The buckling of flat square plates with central circular holes under in-plane edge compression has been studied both theoretically and experimentally by various authors (refs. 1–12). The methods of theoretical analysis used by most of the past investigators (refs. 1–3, 5) were the Rayleigh-Ritz minimum energy method and the Timoshenko method (ref. 13). However, except for Schlack (ref. 3) and Kawai and Ohtsubo (ref. 5), the theoretical analysis methods used do not allow the boundary and loading conditions to be precisely defined for larger hole sizes because the stress distributions of the infinite perforated plate are used as the prebuckling stress solution for the finite perforated plate. Thus, most of the earlier buckling solutions are limited to small hole sizes, and are not fit for studying the effects of different plate boundary conditions on the buckling strengths of the finite plates with arbitrarily sized holes using those approximate solutions.

Using the Rayleigh-Ritz method, Schlack (ref. 3) analyzed the buckling behavior of a simply-supported square plate with a circular hole, subjected to uniform edge displacements with three arbitrary displacement functions, and calculated the buckling displacements. The buckling loads were then calculated using the stress-strain relationships. Ritchie and Rhodes (ref. 7) studied the buckling behavior of both square and rectangular simply-supported perforated plates. Their theoretical analysis employed an approximate approach using a combination of Rayleigh-Ritz and finite-element methods. These methods are reasonably accurate for small holes, but lose accuracy when dealing with larger holes. The results of the analysis show that the buckling behavior of perforated rectangular plates is quite different from that of perforated square plates, and that the buckling mode is dependent on the hole size. Kawai and Ohtsubo (ref. 5) also studied the perforated square plates using the Rayleigh-Ritz procedure with the prebuckling stress distribution determined by the finite-element method. To reduce the labor of numerical calculations, the double integrations in the energy procedure for each finite element were transformed into line integrals around the element boundary using the well-known Gauss theorem.

To minimize the mathematical complexities, Nemeth (refs. 8–11) analyzed perforated square orthotropic plates by converting the classical two-dimensional buckling analysis into an equivalent one-dimensional analysis by approximating the plate displacements with kinematically admissible series. In the analysis, the two unloaded edges were assumed simply supported, and the loaded edges were either simply supported or clamped. This approximate buckling analysis predicted the buckling loads to within 10 percent of those calculated using the finite-element method. Nemeth's analytical and experimental results (ref. 10) indicated that increasing the hole size in a given plate does not always reduce the

buckling load. Using the finite-element method, Lee et al. (ref. 12) examined the buckling behavior of a square plate with a central circular hole. The studies, however, were limited to small hole sizes.

As mentioned earlier, most past theoretical analyses of perforated plates considered mainly the square plates under simply-supported boundary conditions to minimize the mathematical complexities. Likewise, most past experimental studies on perforated plates were limited to square plates under simply-supported boundary conditions because of the need to compare the test data with the existing theoretical results. The past investigations, in general, lack comprehensive information on the buckling behavior of rectangular plates of arbitrary aspect ratios, containing holes of arbitrary sizes, and supported under any specified boundary conditions.

With the availability of powerful tools such as the well-developed, finite-element structural analysis computer programs, it is now possible to calculate the prebuckling stress fields and the buckling eigenvalue solutions quite accurately for the finite rectangular plates of any aspect ratios, containing cutouts of any geometry and any hole sizes, under any specified boundary and loading conditions.

This report investigates the mechanical- and thermal-buckling analyses of rectangular plates containing arbitrarily-sized central circular holes or square holes. A finite-element method was used to study the effects of plate aspect ratio, hole geometry, hole size, and plate boundary conditions on the mechanical- and thermal-buckling strengths of perforated plates.

DESCRIPTION OF THE PROBLEM

The geometry of the perforated rectangular plates and different boundary conditions used in the finite-element analysis are described as follows.

Geometry

Figure 1 shows the geometry of two types of perforated rectangular plates with length l , width w , and thickness t . The central cutout is either a circular hole with diameter d (fig. 1(a)), or a central square hole with side c (fig. 1(b)). Table 1 lists the dimensions of various perforated rectangular plates analyzed. Notice that all the plates have the same width, $w = 20$ in., and the same thickness, $t = 0.1$ in.

Table 1. Dimensions of perforated plates.

w , in.	t , in.	l/w	d/w	c/w
20	0.1	1.0	0 ~ 0.7	0 ~ 0.7
20	0.1	1.5	0 ~ 0.7	0 ~ 0.7
20	0.1	2.0	0 ~ 0.7	0 ~ 0.7

In table 1, the range 0 ~ 0.7 covers 0, 0.05, 0.1, 0.15, 0.2, 0.25, 0.3, 0.35, 0.4, 0.45, 0.5, 0.55, 0.6, 0.65, 0.7. For a given plate aspect ratio, the 15 hole-size cases will provide 15 data points for plotting each buckling curve in the $(N_y)_{cr}$ vs. d/w (or c/w) plots. If the buckling curve has any sharp bends in certain regions, however, additional data points for d/w (or c/w) values not listed in table 1 were generated to define those sharp bend regions more accurately.

Boundary Conditions

The various boundary conditions considered in the mechanical- and thermal-buckling analyses are described as follows.

Mechanical Buckling

For mechanical buckling (uniaxial compressive buckling), the four edges of the perforated plates are either simply supported or clamped. The lower edge of the plate is kept stationary and the upper edge is allowed to move freely in the loading direction (y-direction). The two unloaded edges are either constrained from the transverse in-plane motions (figs. 2(a) and 3(a)) (called fixed case), or unconstrained from the transverse in-plane motions (figs. 2(b) and 3(b)) (called free case). The four cases of boundary conditions considered in the analysis are as follows:

1. 4S fixed—four edges simply supported; the two side edges can slide freely along the lubricated fixed guides (fig. 4(a)).
2. 4S free—four edges simply supported; the two side edges can slide freely along the lubricated guides, which can have free in-plane transverse motions (fig. 4(b)).
3. 4C fixed—four edges clamped; the two side edges can slide freely along the lubricated fixed clamping guides (fig. 5(a)).
4. 4C free—four edges clamped; the two side edges can slide freely along the lubricated clamping guides, which can have free in-plane transverse motions (fig. 5(b)).

Thermal Buckling

For thermal buckling, the plates were subjected to uniform temperature loading. Two types of plate boundary conditions were considered:

1. 4S fixed—four edges simply supported by fixed-edge supports (fig. 6(a)).
2. 4C fixed—four edges clamped by fixed-edge supports (fig. 6(b)).

FINITE-ELEMENT ANALYSIS

In the finite-element analysis, the structural performance and resizing (SPAR) finite-element computer program (ref. 14) was used. Because of symmetry, only one quarter of the perforated plates were modeled. The plates with circular holes were modeled with both triangular combined membrane and bending elements (E33 elements) and quadrilateral combined membrane and bending elements (E43 elements). For the plates with square holes, only the square-shaped E43 elements were used. Two typical quarter-panel finite-element models generated for a typical circular cutout case ($l/w = 1.5$; $d/w = 0.2$) and a typical square cutout case ($l/w = 1.5$; $c/w = 0.2$) are shown, respectively, in figures 7 and 8.

For the circular hole cases, models with aspect ratio $l/w = 2$ were generated by adding 100 additional square E43 elements to the square models ($l/w = 1$); and models with aspect ratio $l/w = 1.5$ were generated by properly modifying the aspect ratio of those additional E43 elements in the models with $l/w = 2$.

Models with circular holes ranging from small to moderate sizes (called the basic models) were generated by modifying the hole sizes without changing the number of elements in the annular domains around the holes (fig. 7). By using this simple method of generating multiple models, the tangential-to-radial aspect ratios of the elements in the annular domains will gradually increase with the increasing size of the holes. Therefore, the models with large circular holes were generated from the basic models by carving out some elements in the hole boundary regions of the basic models. Thus, creating larger holes would hardly disturb the aspect ratios of the elements lying in the remaining annular domains. When the circular holes diminish, 20 additional E33 elements were used to fill each hole cavity so that the models could represent unperforated solid plates.

For the square-hole cases, all the models were generated from the solid plate models (basic models; $c/w = 0$), which have the highest number of joint locations (JLOCs) and E43 elements. The models with different hole sizes were then generated from the basic models by removing the proper number of the square E43 elements around the square-hole boundaries. Also, to increase the model aspect ratios, more square E43 elements were added to the square models.

Table 2 lists the sizes of the basic finite-element models from which numerous perturbed models were generated.

Table 2. Sizes of the basic finite-element models.

l/w	Circular hole ($0 < d/w < 0.6$)			Square hole ($c/w = 0$)*	
	JLOC	E33	E43	JLOC	E43
1.0	951	32	271	441	400
1.5	1061	32	371	651	600
2.0	1061	32	371	861	800

*Number of JLOC and E43 is maximum when $c/w = 0$.

The material properties used in the finite-element analysis are those of monolithic Ti-6Al-4V titanium alloy (ref. 15), listed in table 3.

Table 3. Material properties of Ti-6Al-4V titanium alloy (ref. 15).

	70 °F	200 °F	300 °F	400 °F	500 °F	600 °F	700 °F	800 °F	900 °F	1000 °F
E , $\text{lb/in}^2 \times 10^6$	16.0	15.28	14.80	14.40	14.02	13.63	13.15	12.64	11.84	10.56
G , $\text{lb/in}^2 \times 10^6$	6.20	5.83	5.65	5.50	5.37	5.20	5.02	4.82	4.52	4.03
ν	0.31	0.31	0.31	0.31	0.31	0.31	0.31	0.31	0.31	0.31
α , $\text{in/in-}^\circ\text{F} \times 10^{-6}$	4.85	5.00	5.10	5.19	5.27	5.36	5.44	5.52	5.59	5.62

The data in table 3 are plotted in figure 9 to show the nonlinearity of the temperature-dependent material properties.

MATERIAL PROPERTY ITERATIONS

In the thermal-buckling analysis, calculations of buckling temperatures require material property iterations. Figure 10 shows a graphical iteration process for finding the buckling temperatures ΔT_{cr} for a typical case of a square panel ($l/w = 1$) with circular hole size $d/w = 0.7$ under a 4S free boundary condition. The buckling temperature ΔT_{cr} is plotted against the assumed material temperature T_a . The 45-deg line represents the solution line for the buckling temperature ΔT_{cr} .

For example, if the assumed material temperature T_a agrees with the calculated buckling temperature $\Delta T_{cr} + T_r$ ($T_r = 70$ °F), then the data point of ΔT_{cr} will fall right on the 45-deg solution line. In the first iteration, the material properties at room temperature, $(T_a)_1 = T_r$, were used to calculate the first buckling temperature $(\Delta T_{cr})_1$. The second iteration then uses the material properties at any other temperature, say $(T_a)_2 = 200$ °F, to update the input material properties for the calculations of the second buckling temperature $(\Delta T_{cr})_2$. In the third iteration, the two buckling data points $(\Delta T_{cr})_1$ and $(\Delta T_{cr})_2$ were connected with a straight line to locate the intersection point with the 45-deg solution line. Then, this intersection-point temperature was used to update the material properties for the calculations of the third buckling temperature $(\Delta T_{cr})_3$. This iteration process is to continue until the n^{th} calculated buckling temperature $(\Delta T_{cr})_n$ data point falls right on the 45-deg solution line.

From the geometry of figure 10, $(\Delta T_{cr})_3$ may be expressed as a function of $(\Delta T_{cr})_1$ and $(\Delta T_{cr})_2$ as

$$(\Delta T_{cr})_3 = \frac{(\Delta T_{cr})_1}{1 - \frac{(\Delta T_{cr})_2 - (\Delta T_{cr})_1}{(T_a)_2 - (T_a)_1}} \quad (1)$$

For the present material, the $(\Delta T_{cr})_3$ data point (less than 200 °F) would fall practically on the 45-deg solution line, giving an acceptable solution for ΔT_{cr} . Namely, the value of $(\Delta T_{cr})_3$ calculated from the third material iteration would practically agree with that obtained from equation (1) because the material property curves (especially E curve, fig. 9) are almost linear in the range $70 < T < 200$ °F.

RESULTS

The following sections present the results of the finite-element mechanical- and thermal-buckling analysis of rectangular plates with circular and square holes.

Solution Accuracy

For checking the finite-element solution accuracy, the finite-element buckling solutions for simply-supported solid plates (no holes) of different aspect ratios under uniaxial compression were compared with the corresponding classical buckling solutions (ref. 13). Table 4 shows the results. The classical cases actually correspond to the 4S free cases, which are under uniaxial loadings. The 4S fixed cases are slightly under biaxial loadings and, therefore, were not used for solution-comparison purposes.

Table 4. Comparison of finite-element and classical buckling solutions for simply supported rectangular solid plates under uniaxial compression.

l/w	Buckling mode	$(N_y)_{cr}$, lb/in.		
		Circular hole model ($d = 0$)	Square hole model ($c = 0$)	Timoshenko (ref. 13)
1.0	Symmetrical	145.5983	145.5858	145.5854
1.5	Antisymmetrical	157.9806	157.9707	157.9703
2.0	Antisymmetrical	145.5891	145.5866	145.5854

The very close correlation of the finite-element and the classical buckling solutions shown in table 4 indicates the adequacy of the finite-element modeling, and provides great confidence in the accuracy of the finite-element buckling solutions for the perforated plates presented in this report.

Plates With Circular Holes

For plates with circular holes, three cases are considered: mechanical buckling fixed, mechanical buckling free, and thermal buckling.

Mechanical Buckling for Fixed-Boundary Cases

Figures 11–16, respectively, show the compressive buckling loads $(N_y)_{cr}$ plotted as functions of hole size d/w (figs. 11, 13, and 15), and the associated buckling mode shapes (figs. 12, 14, and 16) for the plates with circular holes under 4S fixed and 4C fixed boundary conditions. Only figure 11 shows typical finite-element buckling solution data points.

For the 4S fixed cases, the antisymmetrical buckling curves always lie considerably above the symmetrical buckling curves for all plate aspect ratios (figs. 11, 13, and 15), and therefore, the buckling mode shapes are always symmetrical (figs. 12(a), 14(a), and 16(a)). The actual buckling loads $(N_y)_{cr}$ (symmetrical) for all plate aspect ratios monotonically decrease slightly from their respective solid plate values as the hole sizes increase (figs. 11, 13, and 15).

For the 4C fixed cases, the symmetrical and antisymmetrical buckling curves entangle each other (or mutually intersect), causing the actual buckling curves (for the lowest $(N_y)_{cr}$ values) to be composite curves consisting of symmetrical and antisymmetrical buckling curves segments. Thus, the buckling mode shapes could be either symmetrical or antisymmetrical (figs. 12(b), 14(b), and 16(b)) depending on the hole sizes and the plate aspect ratios. For larger holes, the secondary or local buckling modes start to appear at the hole boundaries (figs. 12(b), 14(b), and 16(b)).

For a square plate (fig. 11) of the 4C fixed case, the lowest buckling load $(N_y)_{cr}$ decreases from that of the solid plate ($d/w = 0$) as the hole starts to initiate and grow in size. The value of $(N_y)_{cr}$ reaches its minimum value in the vicinity of $d/w = 0.2$, and then continues to increase and changing buckling mode at larger hole sizes. Beyond $d/w = 0.4$, the buckling load $(N_y)_{cr}$ becomes greater than that of the solid square plates ($d/w = 0$).

For rectangular plates (figs. 13 and 15) of the 4C fixed cases, the composite buckling curves are wavy and bent upward as the hole size increases. The lowest buckling loads $(N_y)_{cr}$ increase initially as the holes start to grow in size, then changed mode and reached their respective minimum values near the hole size $d/w = 0.2$. Beyond hole size $d/w = 0.3$, the $(N_y)_{cr}$ values exceed their respective values of the solid rectangular plates ($d/w = 0$). The degrees of increases in the $(N_y)_{cr}$ values for the rectangular plates (figs. 13 and 15), however, are not as pronounced as the square plate case (fig. 11).

Mechanical Buckling for Free-Boundary Cases

Figures 17–22, respectively, show the changes of the compressive buckling loads $(N_y)_{cr}$ with hole size d/w (figs. 17, 19, and 21) and the associated buckling mode shapes (figs. 18, 20, and 22) of the plates with circular holes under 4S free and 4C free boundary conditions. The symmetrical and antisymmetrical buckling curves intersect at certain hole sizes (figs. 17, 19, and 21). For the 4C free cases, the buckling mode shapes of the plates with larger holes (figs. 18, 20, and 22) show complex buckling modes consisting of global and pronounced local buckling at the hole boundaries.

For a square plate (fig.17, which represents the most extensively studied geometry), the buckling loads $(N_y)_{cr}$ for both 4S free and 4C free cases decrease monotonically with the hole size and never increase with the hole size like the 4C fixed case (fig. 11).

For rectangular plates (figs. 19 and 21), the buckling loads $(N_y)_{cr}$ for both the 4S free and 4C free cases increase at larger hole sizes. This effect is more conspicuous for the 4C free cases (especially for aspect ratio $l/w = 2$, shown in fig. 21) than for the 4S free cases.

Thermal Buckling

Figures 23–28 show the buckling temperatures ΔT_{cr} , plotted as functions of the hole size d/w (figs. 23, 25, and 27), and the associated buckling mode shapes (figs. 24, 26, and 28) for the plates with circular holes. The lowest buckling temperatures ΔT_{cr} decrease slightly, as the hole size grows initially, and then increase at larger hole sizes. This effect is more pronounced for the 4C cases than for the 4S cases. The increase of ΔT_{cr} at larger hole sizes is the most pronounced for the square plates under 4C boundary condition (fig. 23), and the value of ΔT_{cr} at hole size $d/w = 0.7$ reaches as high as five times the value of ΔT_{cr} of the unperforated square plate ($d/w = 0$).

Plates With Square Holes

Analyses of plates with square holes were also made for the three case types: mechanical buckling fixed, mechanical buckling free, and thermal buckling.

Mechanical Buckling for Fixed-Boundary Cases

Figures 29–34, respectively, show the variations of the compressive buckling loads $(N_y)_{cr}$ with the increase of the hole size c/w (figs. 29, 31, and 33) and the associated buckling mode shapes (figs. 30, 32, and 34) for the plates with square holes under 4S fixed and 4C fixed boundary conditions. The overall

buckling behavior of plates with square holes is very similar to that of the plates with circular holes. In comparison with the circular hole cases, however, the square hole cases have slightly higher buckling loads at larger hole sizes, especially for the aspect ratio $l/w = 1.5$ (compare 4C fixed cases in figs. 13 and 31). At large hole size (figs. 30, 32, and 34) for 4C cases, the buckling mode shapes exhibit both global and local buckling modes.

Mechanical Buckling for Free-Boundary Cases

Figures 35–40 show the compressive buckling loads $(N_y)_{cr}$ plotted against the hole size c/w (figs. 35, 37, and 39) and the associate buckling mode shapes (figs. 36, 38, and 40), for the plates with square holes under 4S free and 4C free boundary conditions. Again, the buckling behavior of the square hole cases is very similar to that of the corresponding circular hole cases. Similar to the fixed cases, the local buckling modes show up clearly at larger hole sizes under the 4C boundary condition.

Thermal Buckling

Figures 41–46, respectively, show the buckling temperatures ΔT_{cr} as functions of hole size c/w (figs. 41, 43, and 45) and the associated thermal-buckling modes (figs. 42, 44, and 46) for the plates with square holes. Again, the 4C boundary condition causes secondary local buckling modes to show up at large hole size for the square plate (fig. 42). For the rectangular plates (figs. 44 and 46), the local buckling modes are almost invisible.

Comparison of Buckling Strengths

The buckling strengths of the plates with circular holes will be compared with those of the plates with square holes under the same weight density conditions. Therefore, for a given aspect ratio of the perforated plates (no change in width w), the area of the square hole was set equal to that of the circular hole by adjusting the side c of the square hole according to the relationship

$$\frac{c}{d} = \frac{\sqrt{\pi}}{2} \quad (2)$$

Thus, before the comparison of buckling strengths could be made, the abscissa c/w of figures 29, 31, 33, 35, 37, 39, 41, 43, and 45 must first be converted to the equivalent d/w using equation (2). Namely, the data points for the square hole cases must be shifted slightly toward the right because the equivalent d/w is slightly greater than c/w in view of equation (2).

Figures 47–49 compare the compressive buckling strengths of the two types of perforated plates under 4S fixed and 4C fixed conditions. At large hole sizes, the square hole cases exhibit higher buckling strengths than the respective circular hole case.

For the 4S free and 4C free boundary conditions, the square plates with square holes (fig. 50) have higher compressive buckling strengths than those with circular holes. For the perforated rectangular plates (figs. 51 and 52), the square hole cases give slightly higher buckling strengths at moderate hole sizes than the circular hole cases. The reverse is true, however, for hole sizes greater than $d/w = 0.5$.

Figures 53–55 compare the thermal-buckling strengths of the two types of perforated plates. Again, the plates with square holes exhibit higher thermal-buckling strengths than those with circular holes for all the hole sizes and boundary conditions.

DISCUSSION

The buckling behavior of plates with central holes as presented is quite peculiar because, under certain boundary conditions (especially cases with clamped edges) and plate aspect ratios, the mechanical- and thermal-buckling strengths of the perforated plates, contrary to expectation, increase rather than decrease as the hole sizes grow larger. The conventional wisdom is that, as the hole sizes increase, the plates lose more materials and become weaker. Therefore, the buckling strengths were expected to decrease as the hole sizes increase. This was not the case. Such peculiar buckling phenomenon of the perforated plates may be explained as follows.

When the hole size becomes considerably large relative to the plate width, most of the compressive load is carried by the narrow side strips of material along the plate boundaries. As is well known, a stronger plate boundary condition (e.g., clamped rather than simply-supported boundaries) increases the buckling strength, while the higher stress concentration decreases the buckling strength. Thus, which effects become dominant will determine the increase or decrease of the buckling strengths of the perforated plates.

For the square-hole cases, the load-carrying narrow side strips along the plate boundaries are practically under uniform compressive stress fields. For the circular-hole cases, the narrow compressed side strips are under stress concentration, which reduces the buckling strengths. This fact may explain why, for most of the cases studied (except figs. 51 and 52), the buckling strengths of the plates with square holes increase more at larger hole sizes than the plates with circular holes having the same weight density.

The unusual buckling characteristics of the perforated plates offer vital applications in aerospace structural panel design. Namely, by opening holes of proper sizes in aerostructural panels for weight saving, their buckling strengths can be boosted simultaneously. Thus, with a single stone, one can shoot down two birds.

CONCLUDING REMARKS

Finite-element mechanical- and thermal-buckling analyses were performed on plates containing centrally located circular and square holes. The effects of plate aspect ratio, hole geometry, hole size, and plate support conditions on the mechanical- and thermal-buckling strengths and buckling mode shapes were studied in great detail. The key findings of the analysis are as follows:

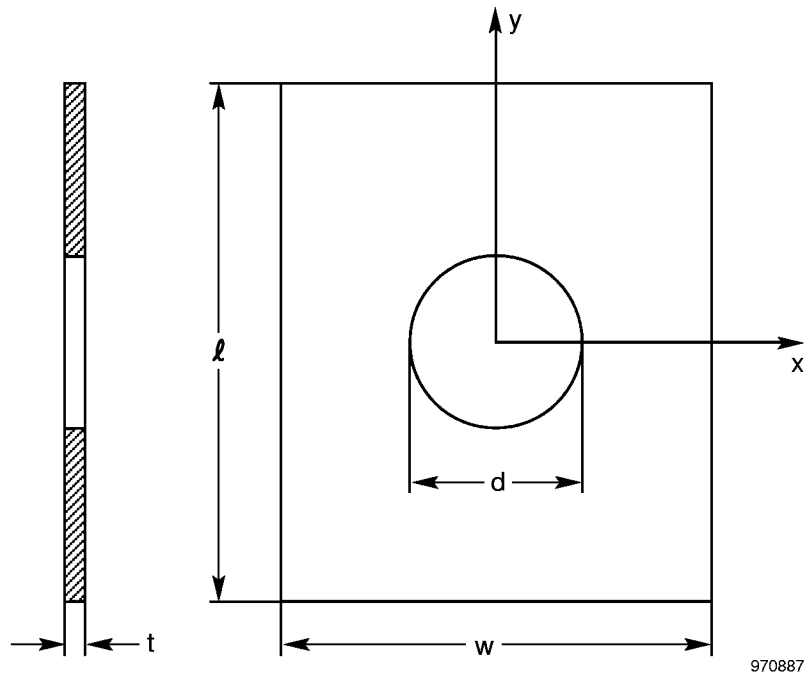
- The buckling mode shapes of the perforated plates can be symmetrical or antisymmetrical depending on the hole sizes, plate aspect ratios, and plate boundary conditions.
- Increasing the hole size does not necessarily reduce the mechanical- and thermal-buckling strengths of the perforated plates. For certain plate aspect ratios and plate support conditions, mechanical- and thermal-buckling strengths increase with the increasing hole sizes.

- For most cases under the same weight density conditions, the mechanical- and thermal-buckling strengths of the plates with square holes are slightly higher than those of the corresponding plates with circular holes at increasing hole sizes.
- The clamped boundary conditions more effectively enhance the mechanical- and thermal-buckling strengths of the perforated plates at larger hole sizes than the simply-supported boundary conditions.

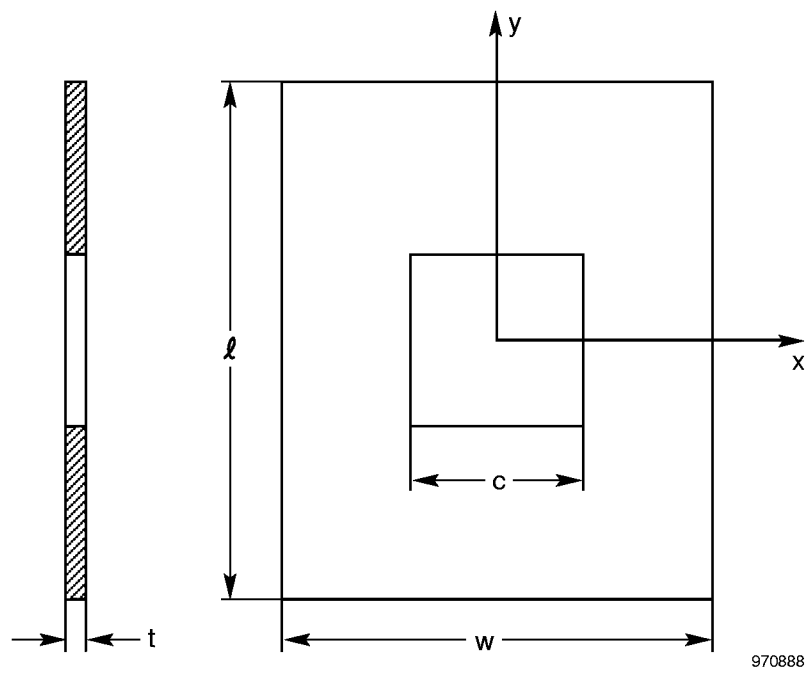
*Dryden Flight Research Center
National Aeronautics and Space Administration
Edwards, California, May 27, 1997*

REFERENCES

1. Levy, Samuel, Ruth M. Woolley, and Wilhelmina D. Kroll, "Instability of Simply Supported Square Plate With Reinforced Circular Hole in Edge Compression," *Journal of Research*, National Bureau of Standards, vol. 39, research paper no. RP1849, Dec. 1947, pp. 571–577.
2. Kumai, Toyoji, "Elastic Stability of the Square Plate With a Central Circular Hole Under Edge Thrust," *Proc. Japan Nat. Cong. Appl. Mech.*, 1951, pp. 81–88.
3. Schlack, A. L., Jr., "Elastic Stability of Pierced Square Plates," *Experimental Mechanics*, June 1964, pp. 167–172.
4. Schlack, Alois L., Jr., "Experimental Critical Loads for Perforated Square Plates," *Experimental Mechanics*, Feb. 1968, pp. 69–74.
5. Kawai, T. and H. Ohtsubo, "A Method of Solution for the Complicated Buckling Problems of Elastic Plates With Combined Use of Rayleigh-Ritz's Procedure in the Finite Element Method," AFFDL-TR-68-150, 1968.
6. Yu, Wei-Wen and Charles S. Davis, "Cold-Formed Steel Members With Perforated Elements," *J. Structural Division*, ASCE, vol. 99, no. ST10, Oct. 1973, pp. 2061–2077.
7. Ritchie, D. and J. Rhodes, "Buckling and Post-Buckling Behaviour of Plates With Holes," *Aeronautical Quarterly*, vol. 26, Nov. 1975, pp. 281–296.
8. Nemeth, Michael Paul, "Buckling Behavior of Orthotropic Composite Plates With Centrally Located Cutouts," Ph. D. Dissertation, Virginia Polytechnic Institute and State University, May 1983.
9. Nemeth, Michael P., *A Buckling Analysis for Rectangular Orthotropic Plates With Centrally Located Cutouts*, NASA TM-86263, Dec. 1984.
10. Nemeth, Michael P., Manuel Stein, and Eric R. Johnson, *An Approximate Buckling Analysis for Rectangular Orthotropic Plates With Centrally Located Cutouts*, NASA TP-2528, Feb. 1986.
11. Nemeth, M. P., "Buckling Behavior of Compression-Loaded Symmetrically Laminated Angle-Ply Plates With Holes," *AIAA Journal*, vol. 26, no. 3, Mar. 1988, pp. 330–336.
12. Lee, Y. J., H. J. Lin, and C. C. Lin, "A Study on the Buckling Behavior of an Orthotropic Square Plate With a Central Circular Hole," *Composite Structures*, vol. 13, no. 3, 1989, pp. 173–188.
13. Timoshenko, Stephen P. and James M. Gere, *Theory of Elastic Stability*, 2nd ed., McGraw-Hill Book Company, New York, 1961.
14. Whetstone, W. D., *SPAR Structural Analysis System Reference Manual: System Level 13A, vol. 1, Program Execution*, NASA CR-158970-1, Dec. 1978.
15. U.S. Government, Military Handbook 5B (MIL-HDBK-5B), Aug. 31, 1973.

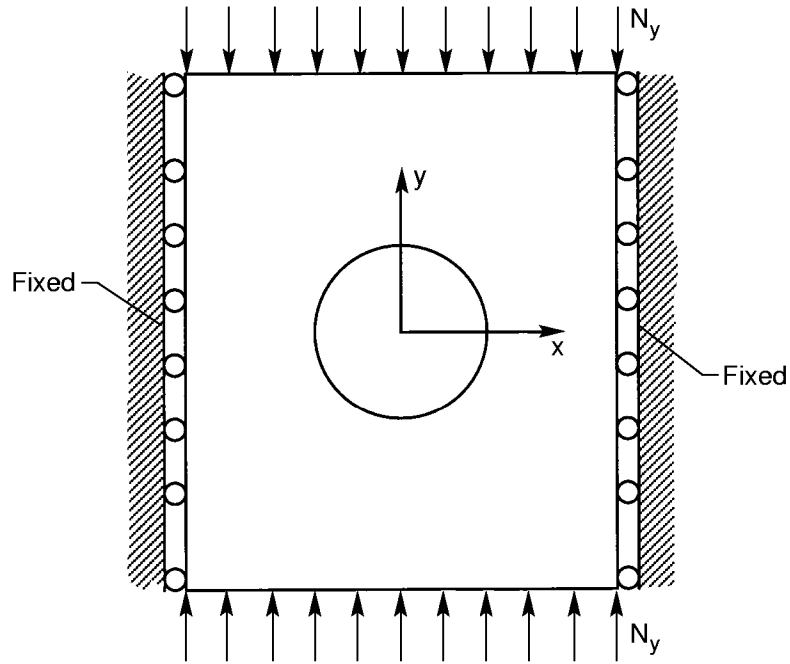


(a) Circular cutout.



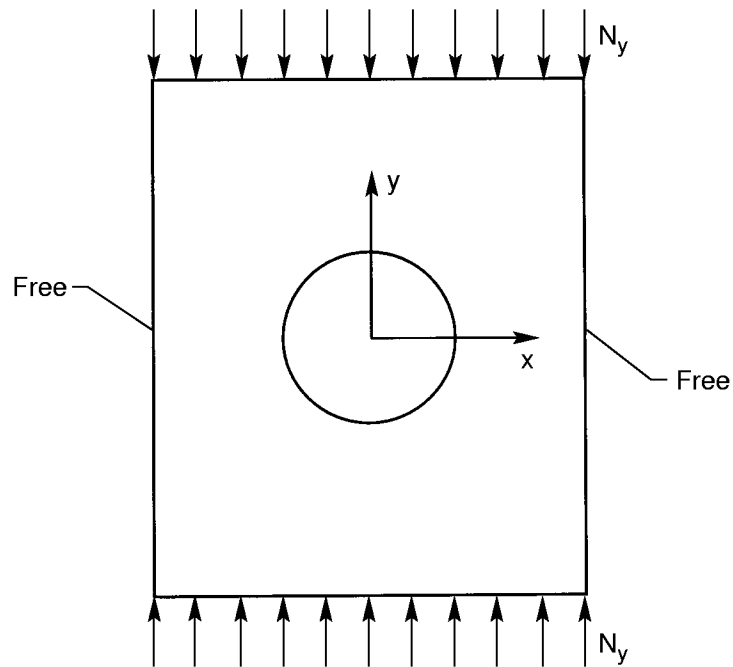
(b) Square cutout.

Figure 1. Rectangular plates with central cutouts.



970889

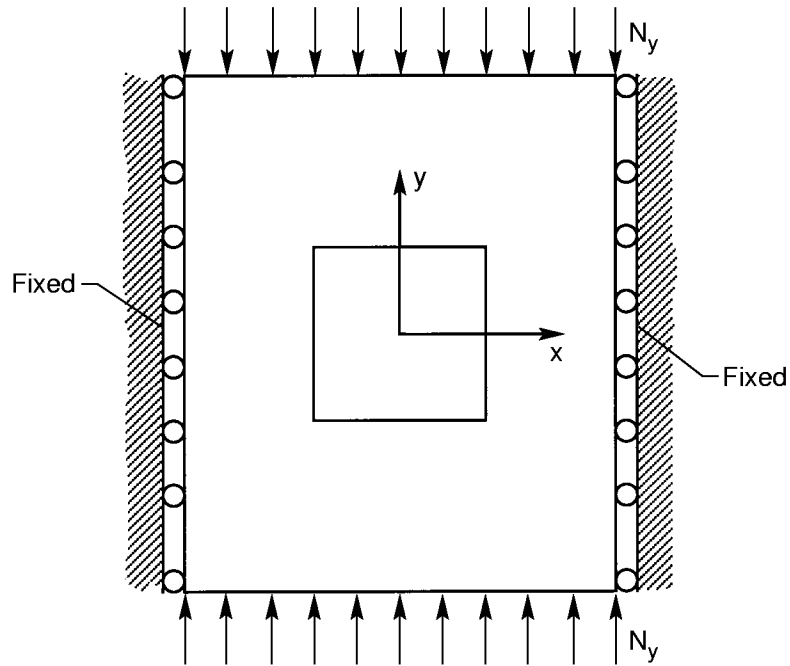
(a) Fixed case—two vertical edges with no in-plane transverse motions.



970890

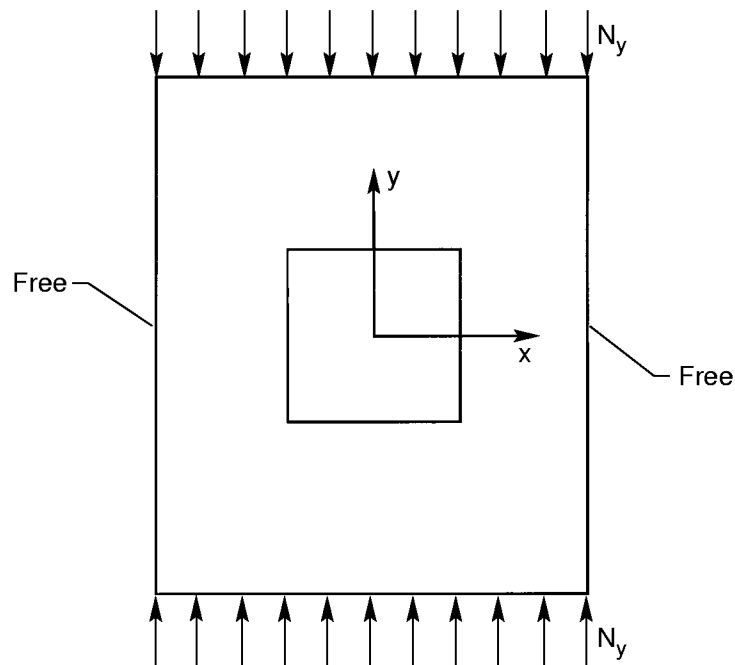
(b) Free case—two vertical edges with free in-plane transverse motions.

Figure 2. Fixed and free boundary conditions for two vertical edges; circular cutout case (simply supported or clamped).



970891

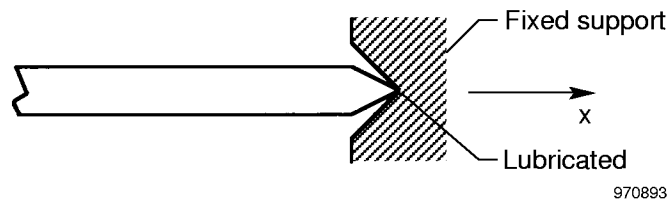
(a) Fixed case—two vertical edges with no in-plane transverse motions.



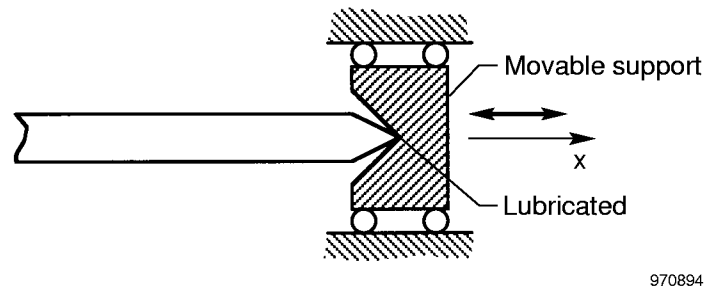
970892

(b) Free case—two vertical edges with free in-plane transverse motions.

Figure 3. Fixed and free boundary conditions for two vertical edges; square cutout case (simply supported or clamped).

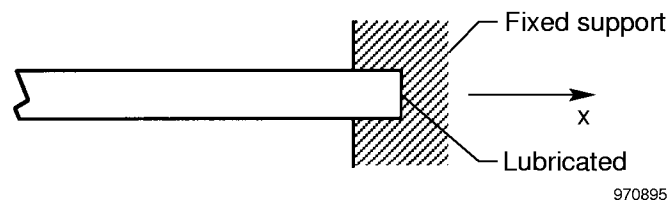


(a) 4S fixed.

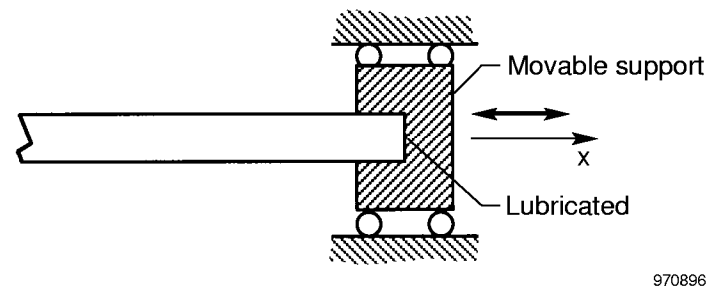


(b) 4S free.

Figure 4. Two types of boundary conditions for simply-supported vertical edges.

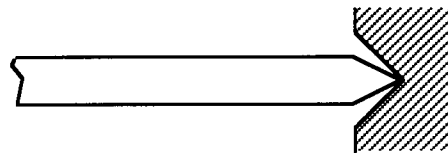
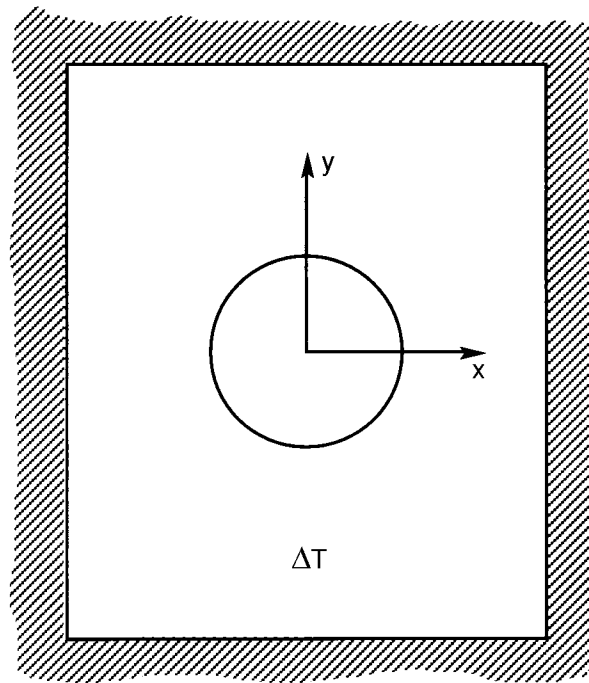


(a) 4C fixed.



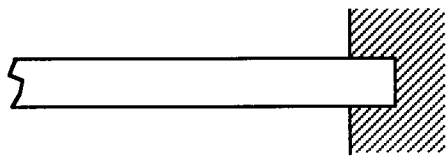
(b) 4C free.

Figure 5. Two types of boundary conditions for clamped vertical edges.



970897

(a) 4S fixed.



970898

(b) 4C fixed.

Figure 6. Two types of boundary conditions used for thermal buckling.

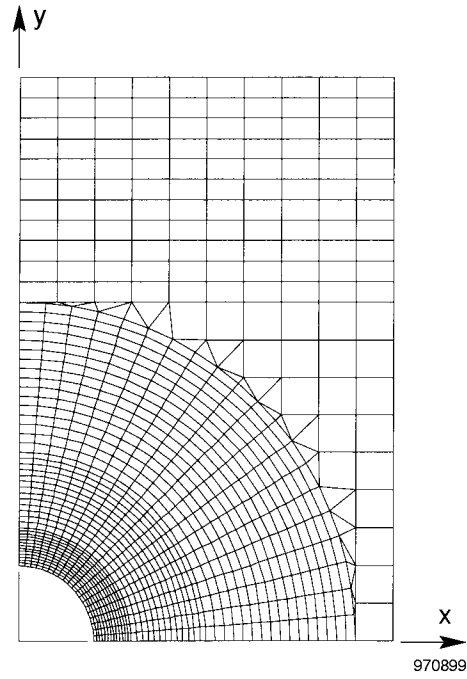


Figure 7. Quarter-panel, finite-element model for rectangular plate with circular hole; $l/w = 1.5$, $d/w = 0.2$.

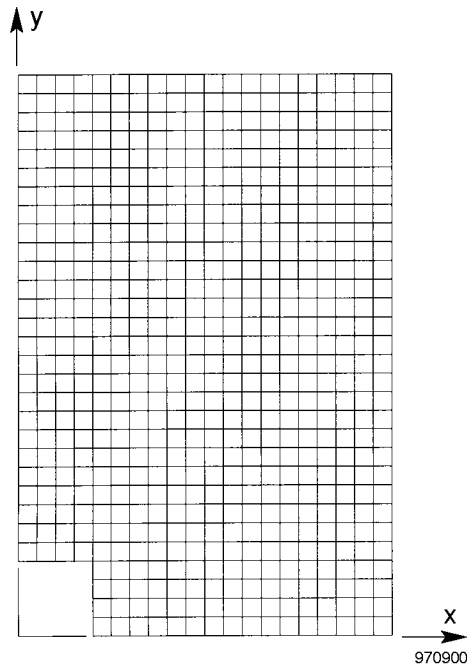


Figure 8. Quarter-panel, finite-element model for rectangular plate with square hole; $l/w = 1.5$, $c/w = 0.2$.

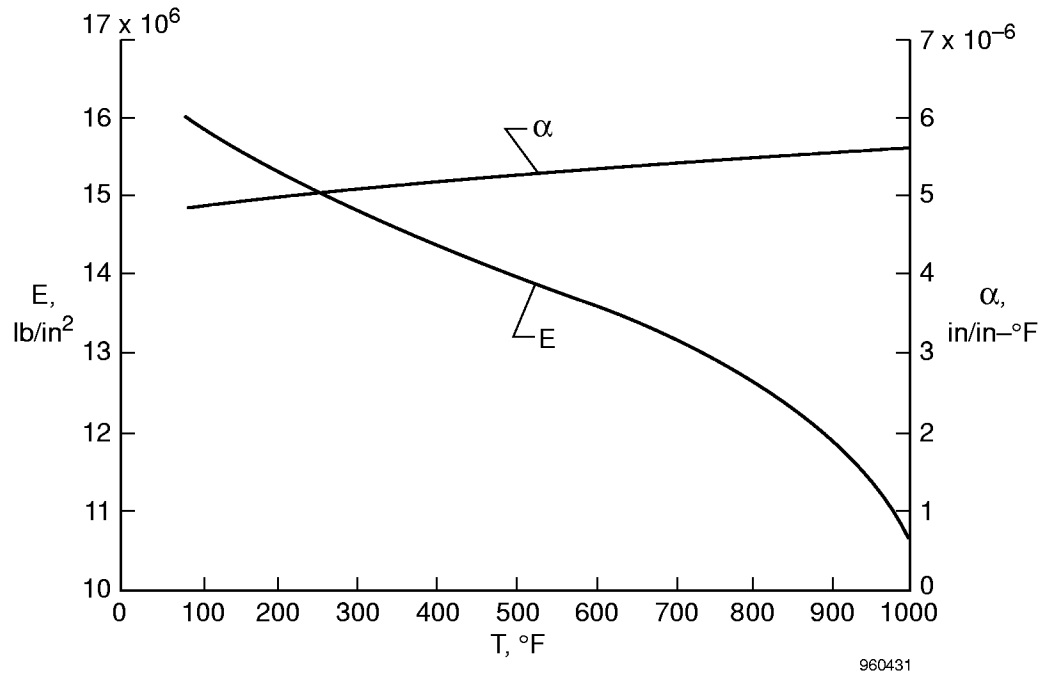


Figure 9. Temperature-dependent material properties of Ti-6Al-4V titanium alloy.

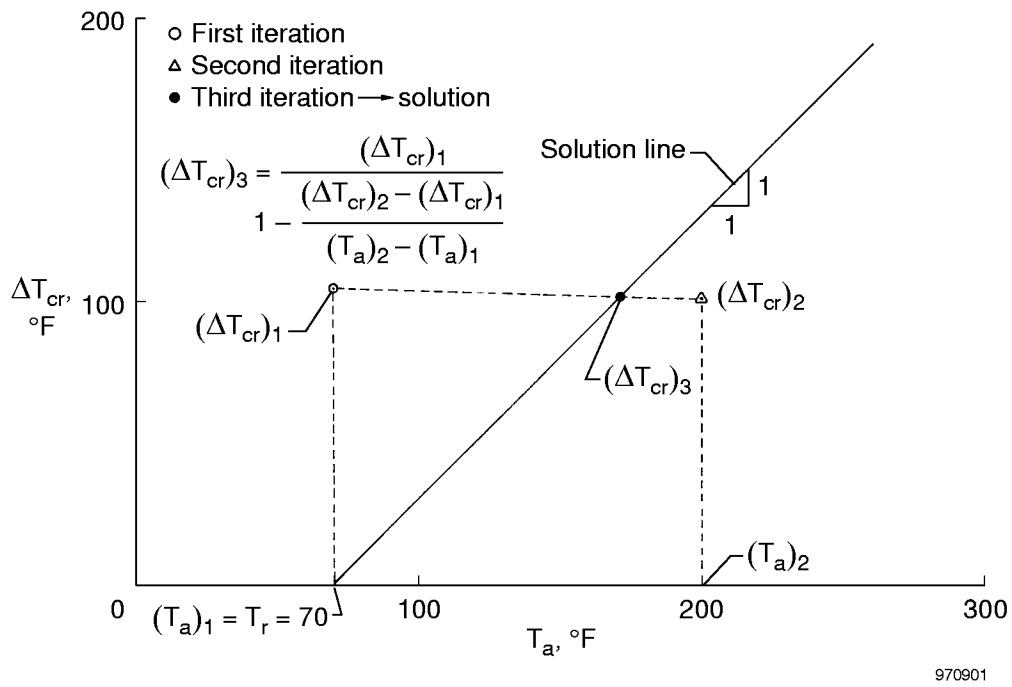


Figure 10. Graphical representation of buckling temperature iteration process.

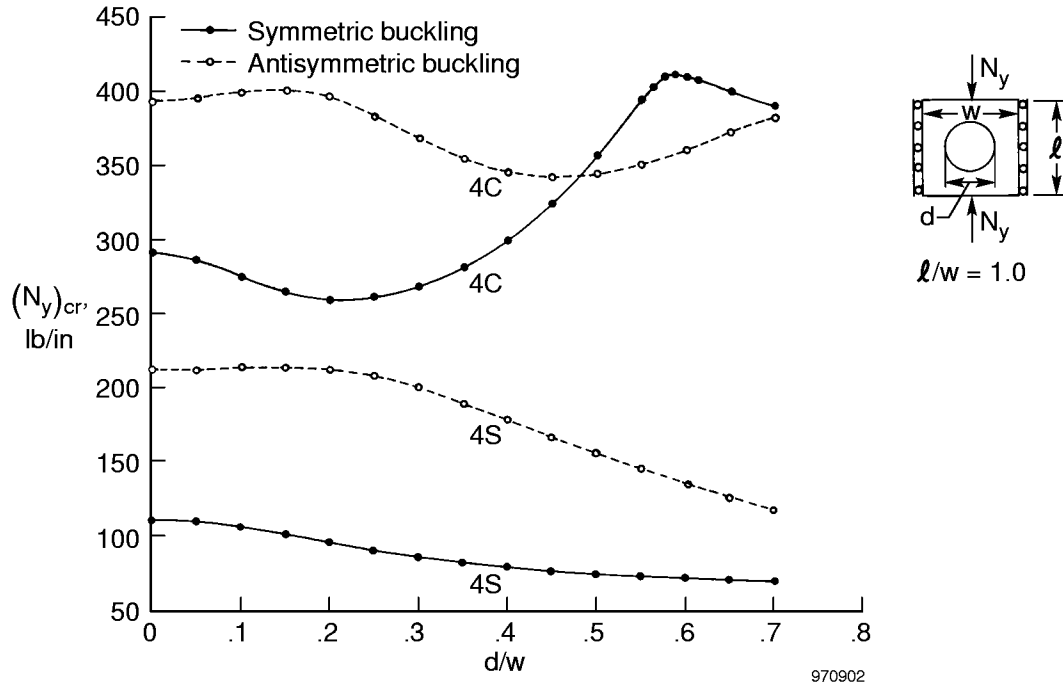


Figure 11. Compressive buckling loads as functions of hole size; circular holes; fixed edges.

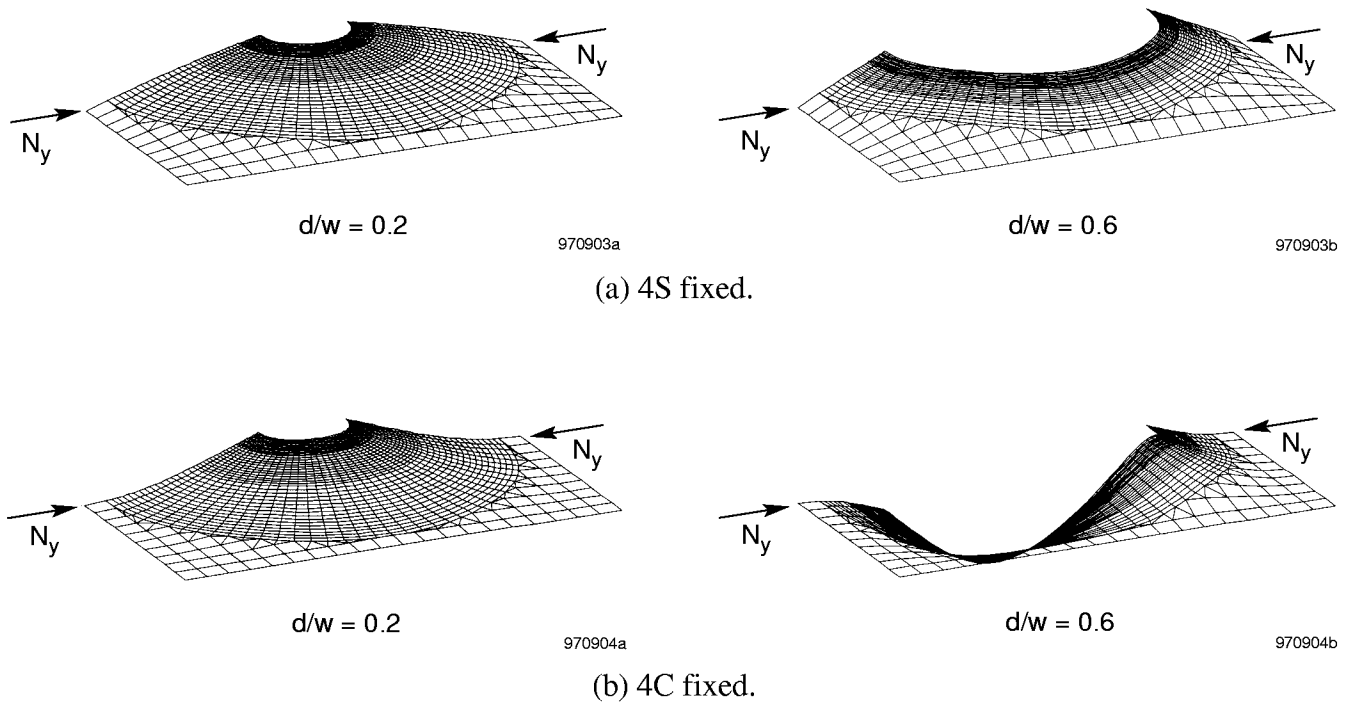


Figure 12. Buckled shapes of square plates with circular holes under compression; $l/w = 1$; fixed edges.

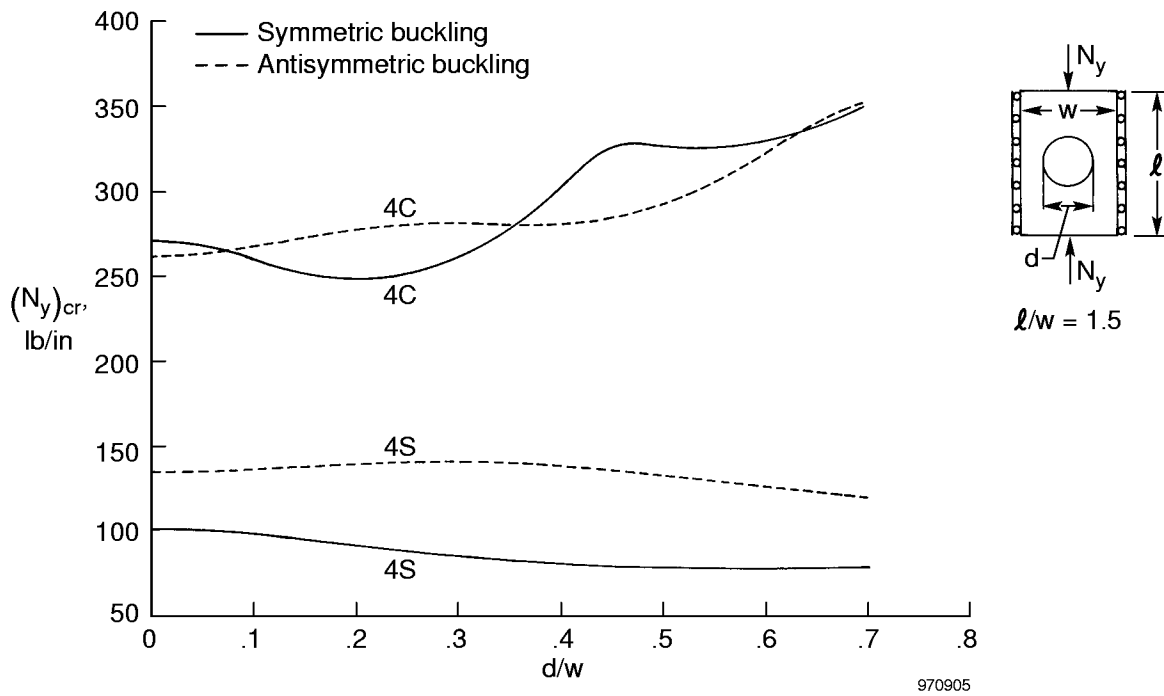


Figure 13. Compressive buckling loads as functions of hole size; circular holes; fixed edges.

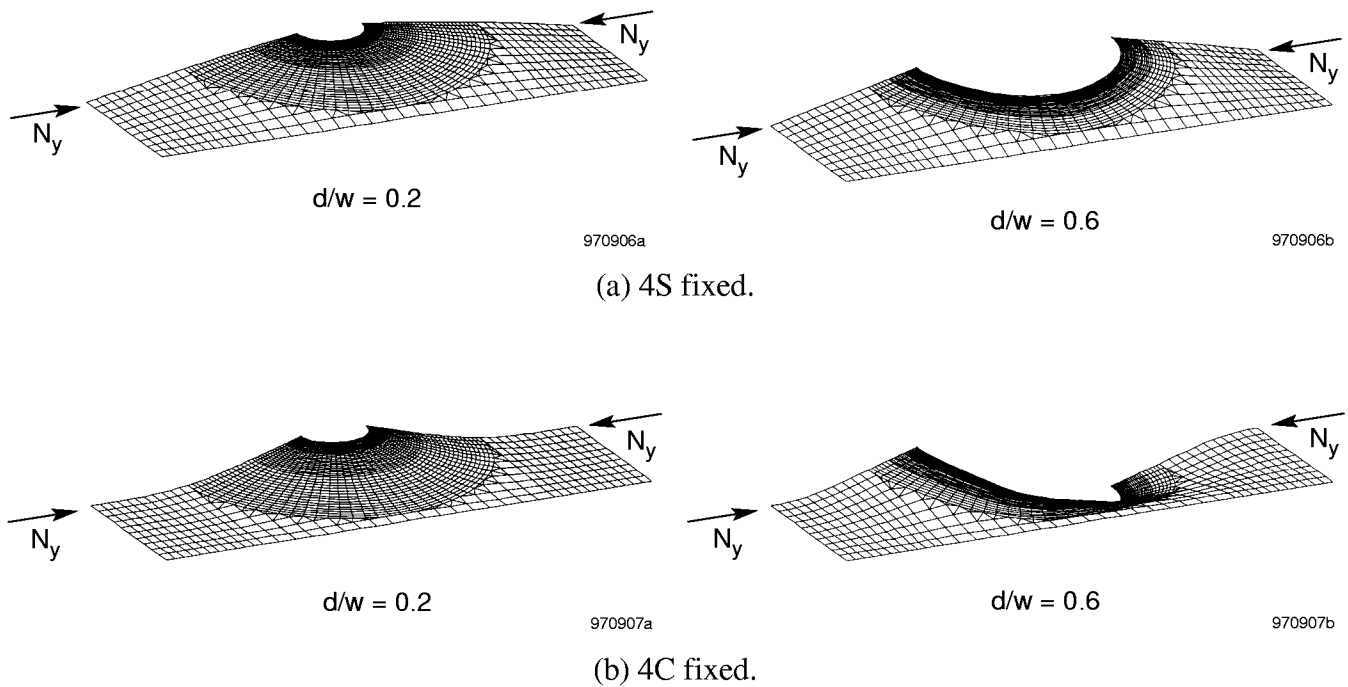


Figure 14. Buckled shapes of rectangular plates with circular holes under compression; $l/w = 1.5$; fixed edges.

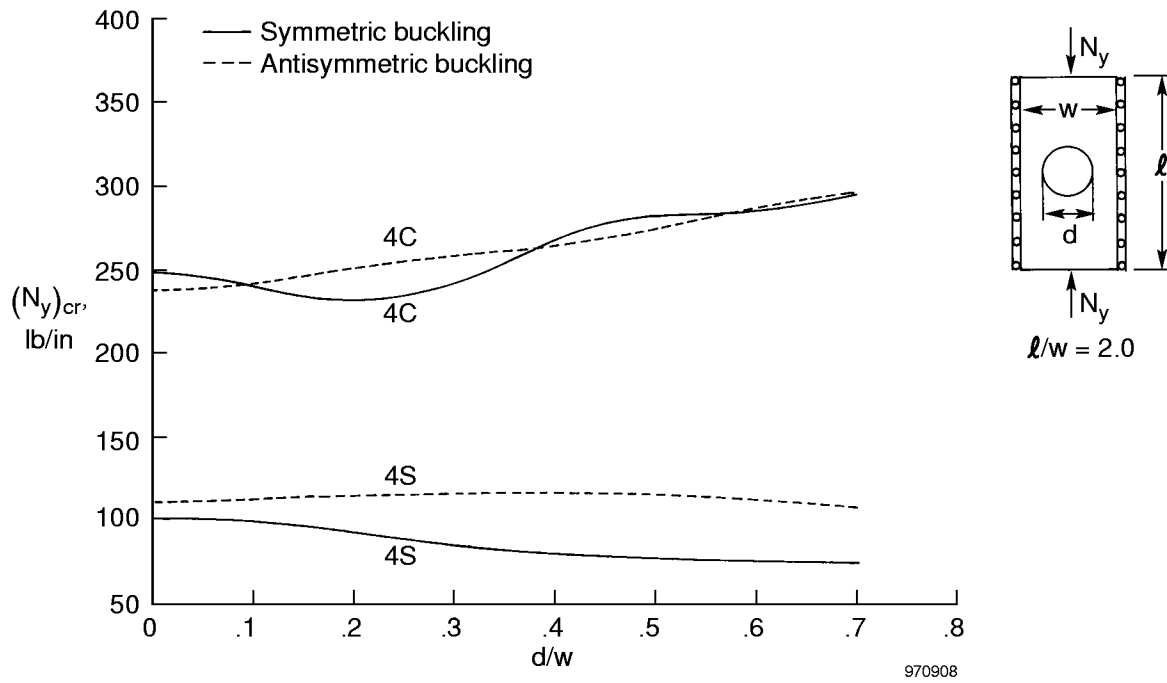


Figure 15. Compressive buckling loads as functions of hole size; circular holes; fixed edges.

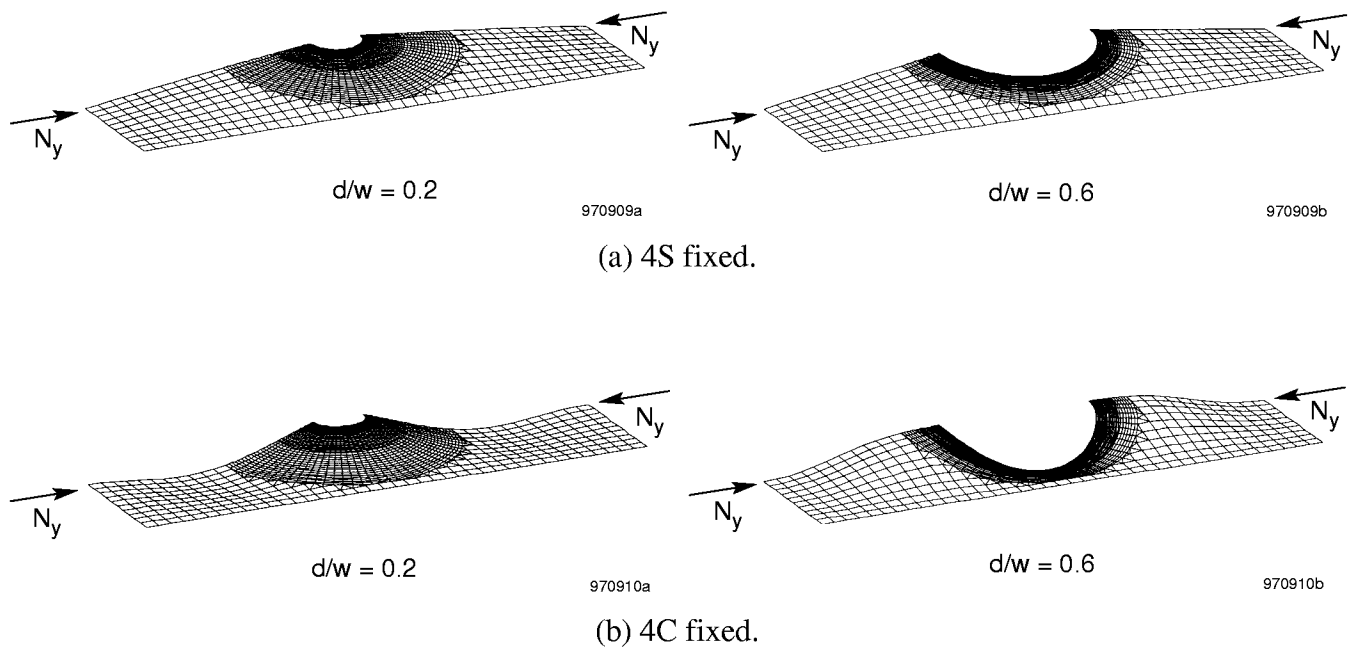


Figure 16. Buckled shapes of rectangular plates with circular holes under compression; $l/w = 2$; fixed edges.

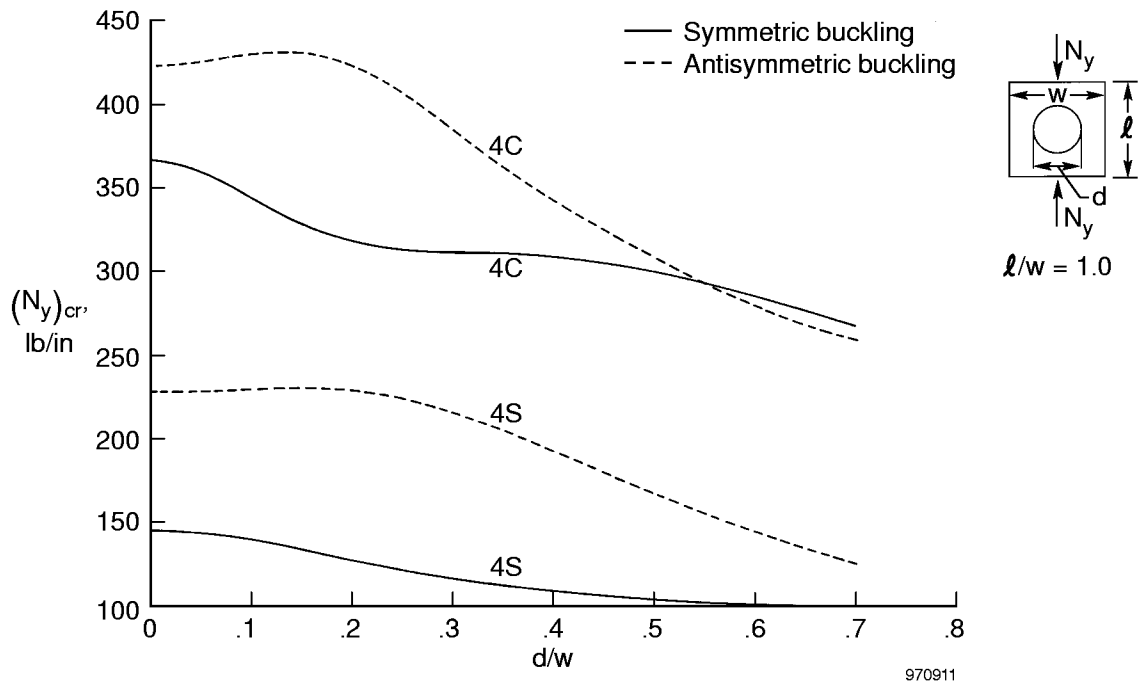


Figure 17. Compressive buckling loads as functions of hole size; circular holes; free edges.

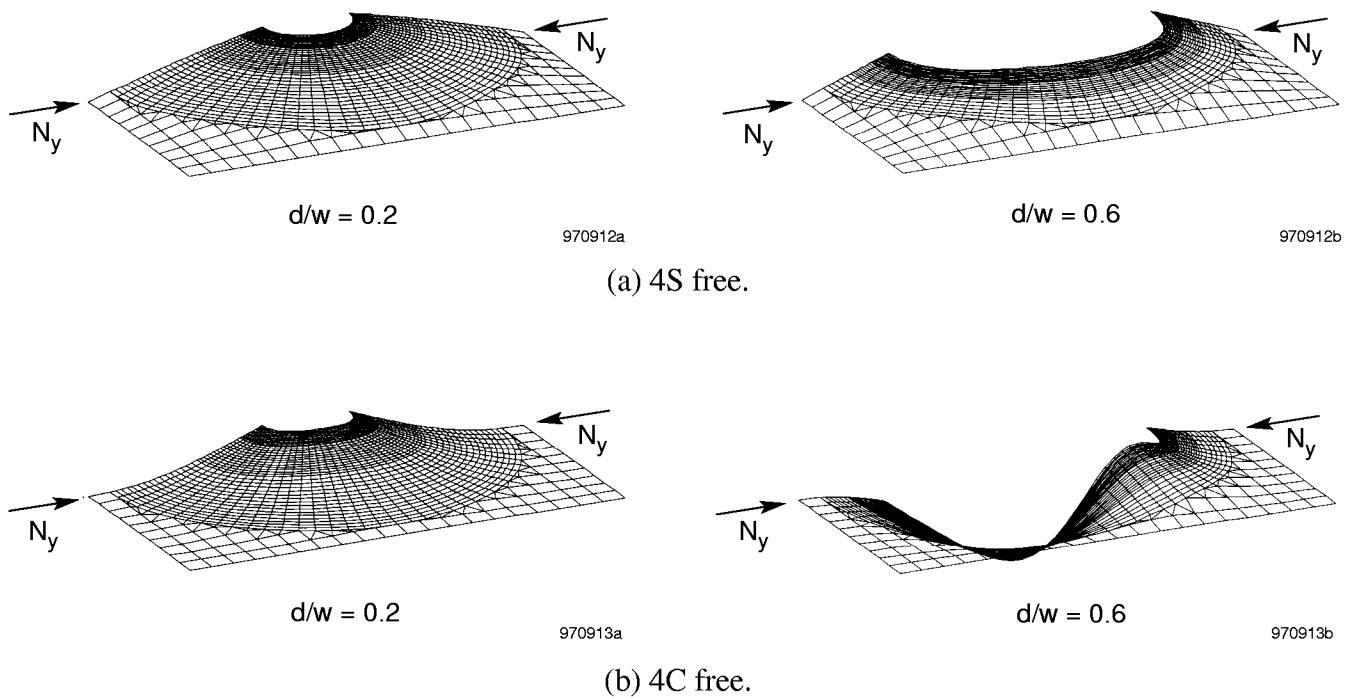


Figure 18. Buckled shapes of square plates with circular holes under compression; $l/w = 1$; free edges.

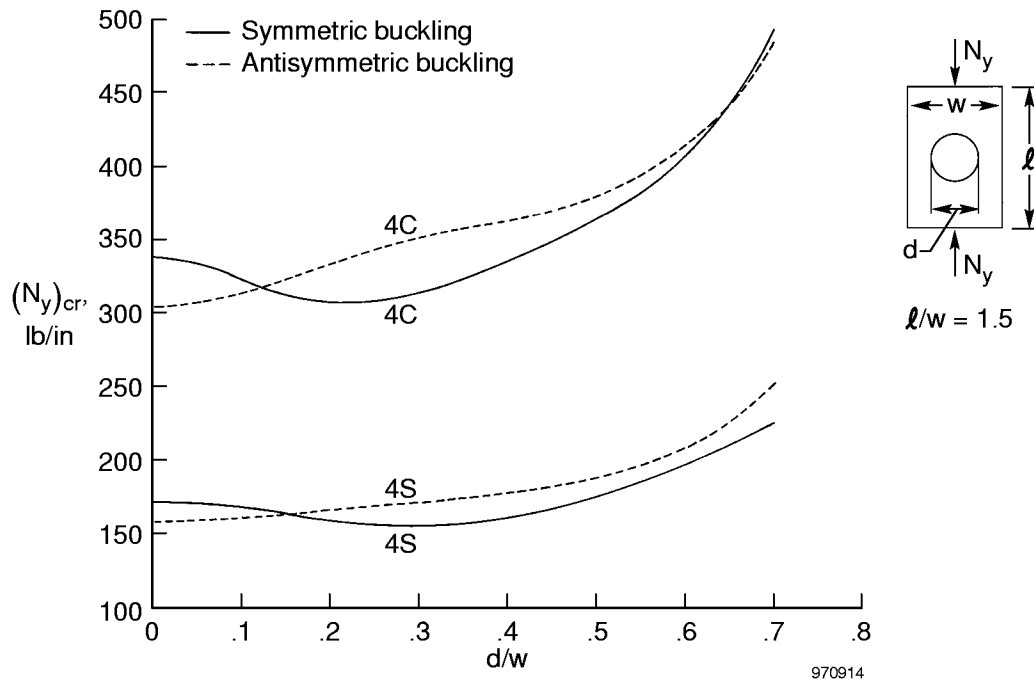


Figure 19. Compressive buckling loads as functions of hole size; circular holes; free edges.

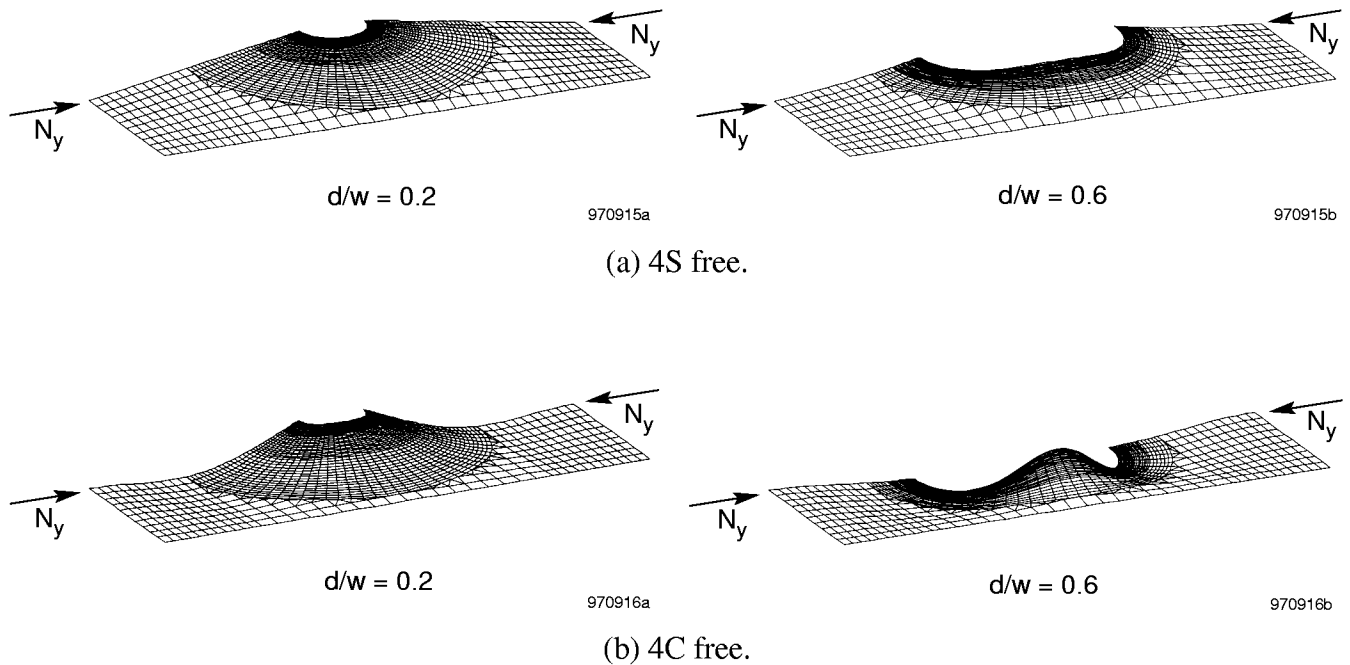


Figure 20. Buckled shapes of rectangular plates with circular holes under compression; $l/w = 1.5$; free edges.

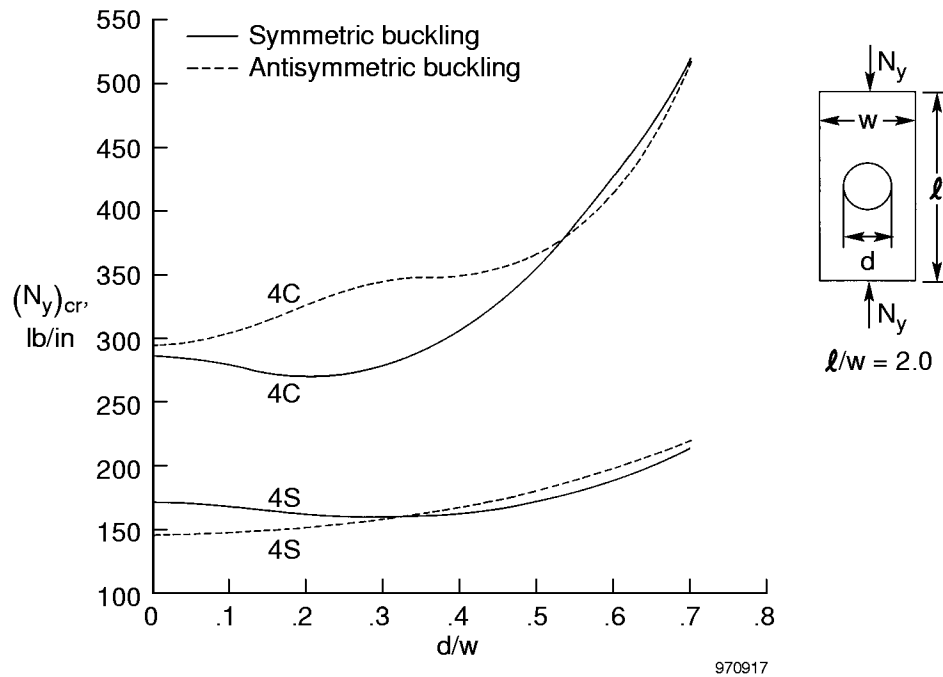


Figure 21. Compressive buckling loads as functions of hole size; circular holes; free edges.

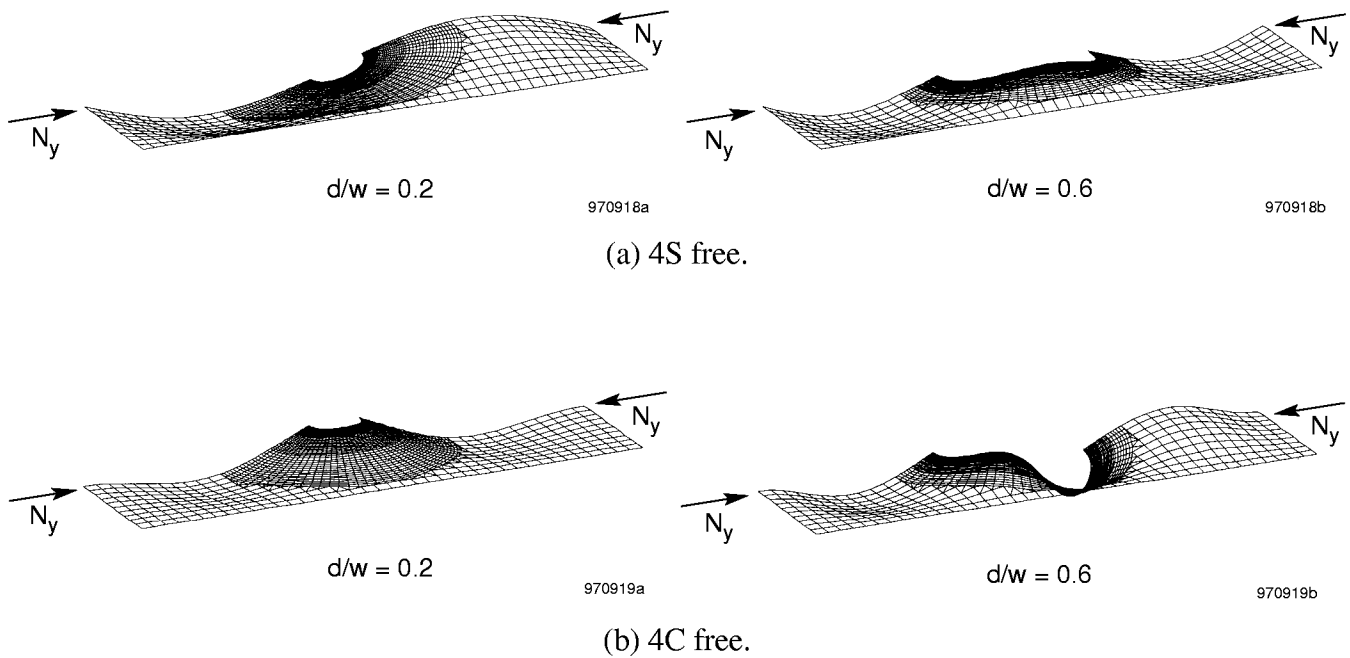


Figure 22. Buckled shapes of rectangular plates with circular holes under compression; $l/w = 2$; free edges.

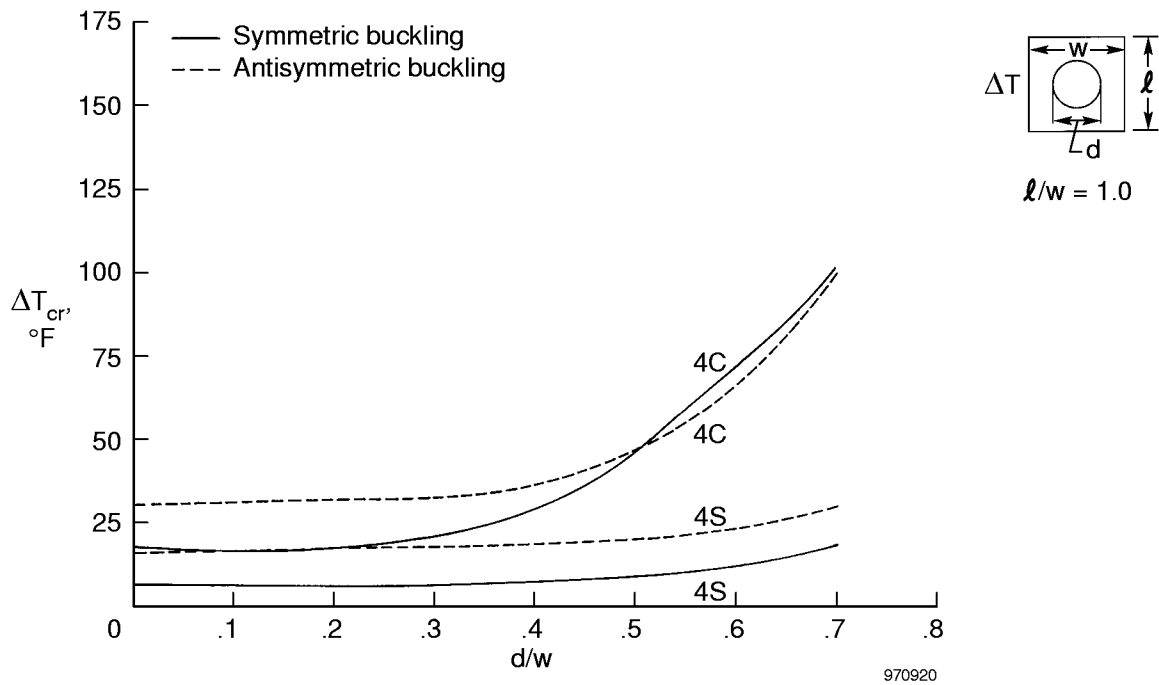
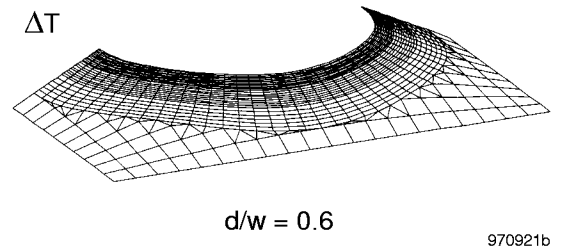
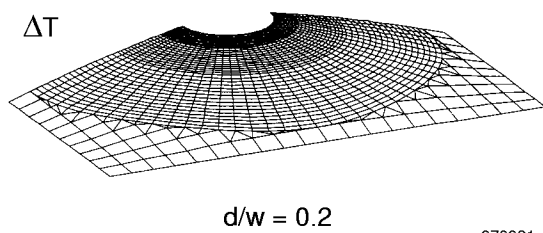
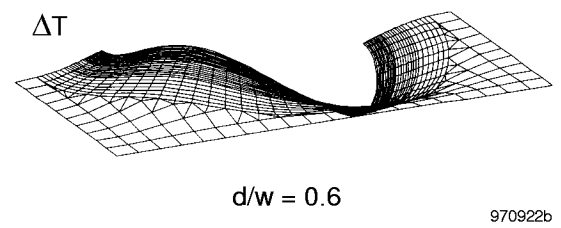
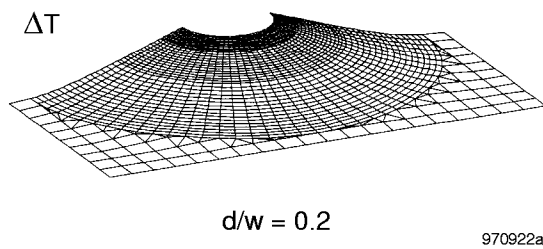


Figure 23. Buckling temperatures as functions of hole size; circular holes.



(a) 4S fixed.



(b) 4C fixed.

Figure 24. Buckled shapes of uniformly heated square plates with circular holes; $l/w = 1$.

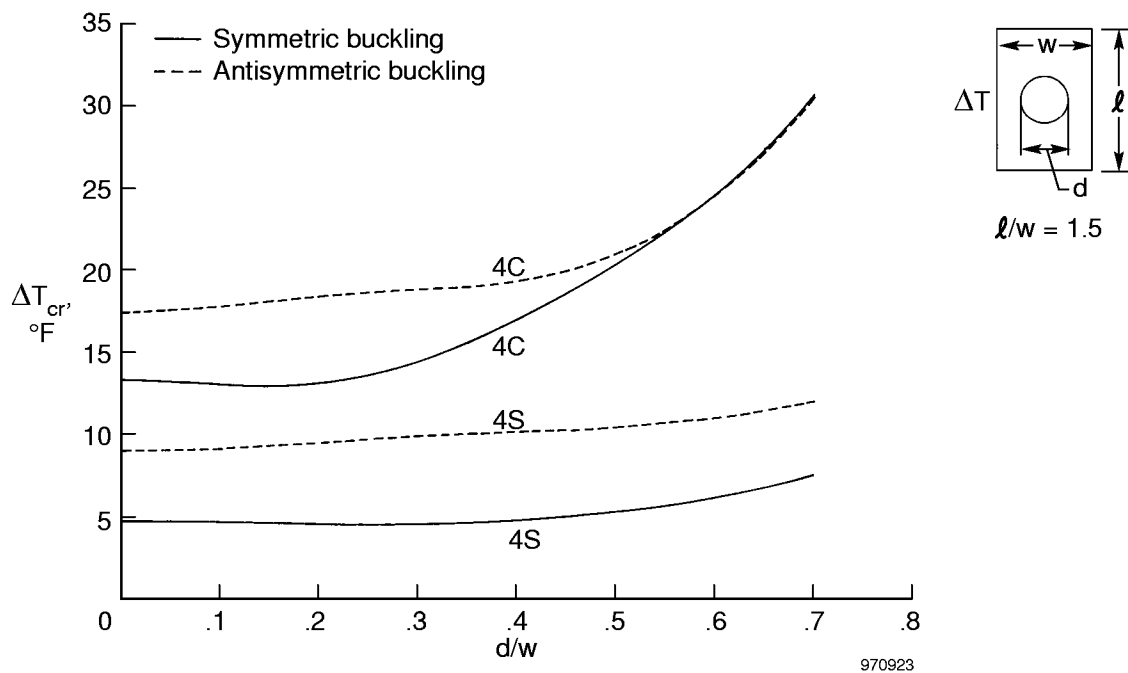
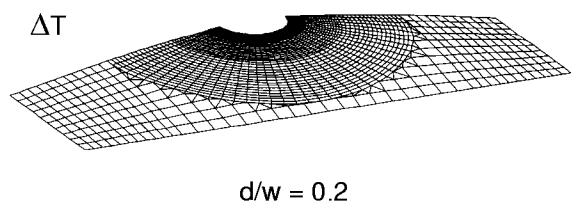
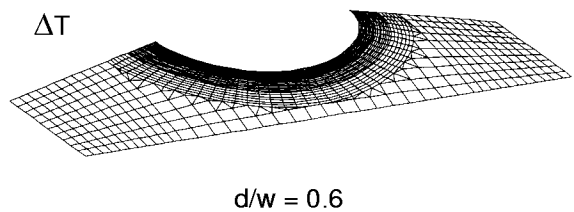


Figure 25. Buckling temperatures as functions of hole size; circular holes.

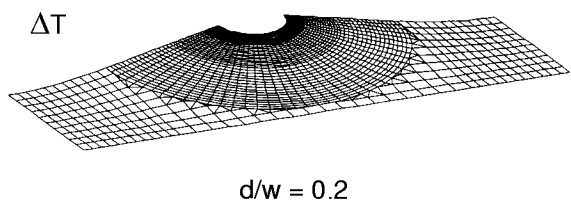


970924a

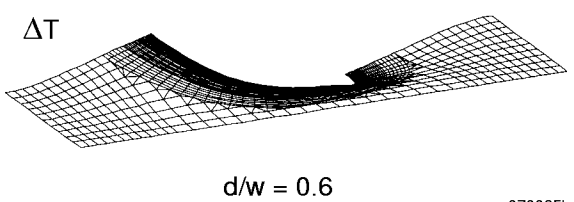


970924b

(a) 4S fixed.



970925a



970925b

(b) 4C fixed.

Figure 26. Buckled shapes of uniformly heated rectangular plates with circular holes; $l/w = 1.5$.

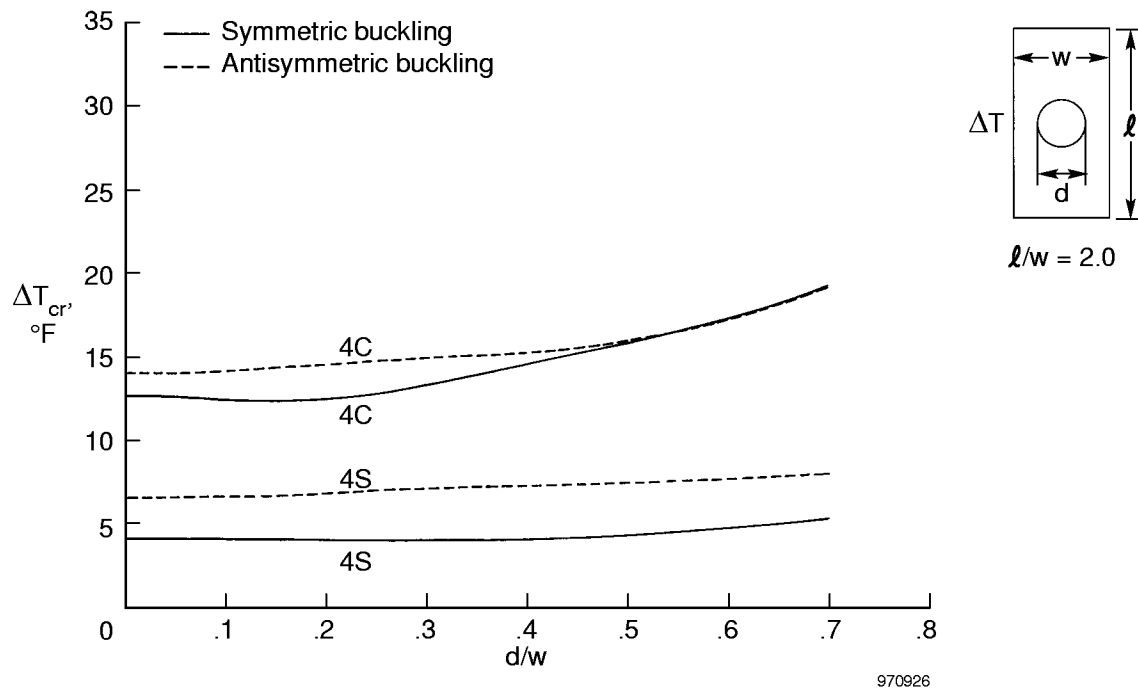


Figure 27. Buckling temperatures as functions of hole size; circular holes.

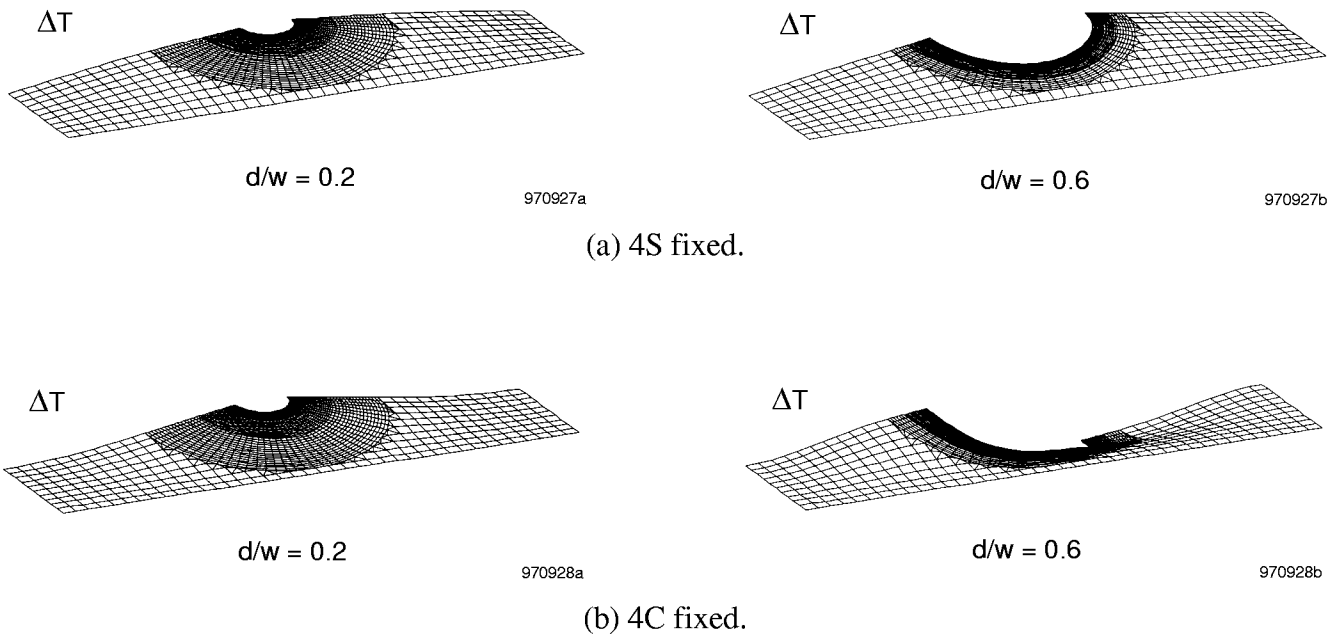


Figure 28. Buckled shapes of uniformly heated rectangular plates with circular holes; $l/w = 2$.

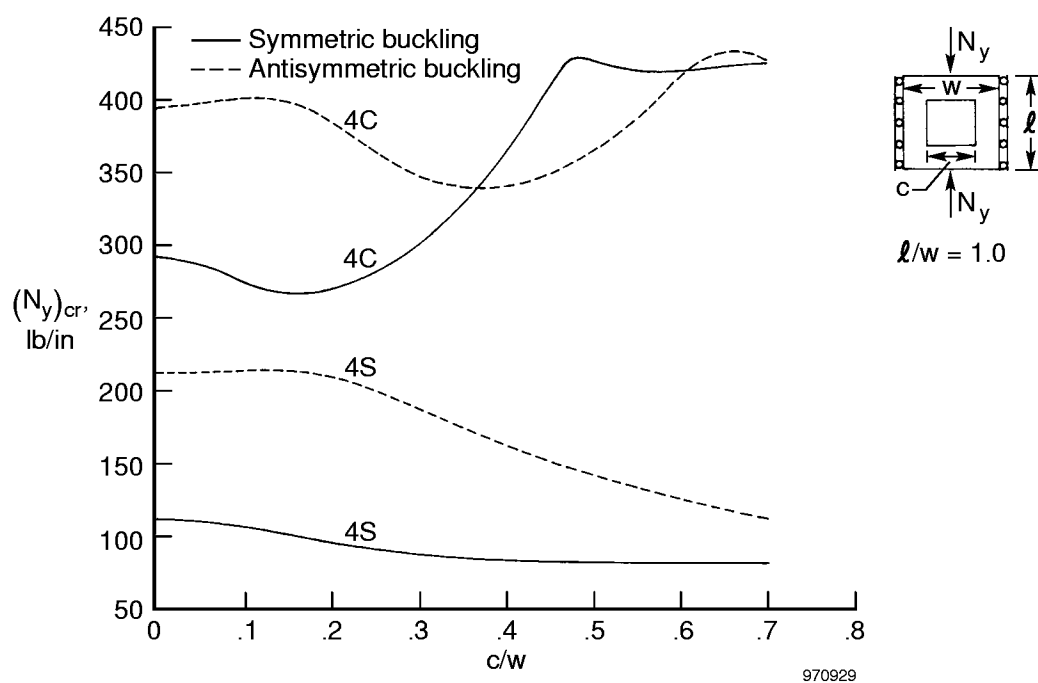


Figure 29. Compressive buckling loads as functions of hole size; square holes; fixed edges.

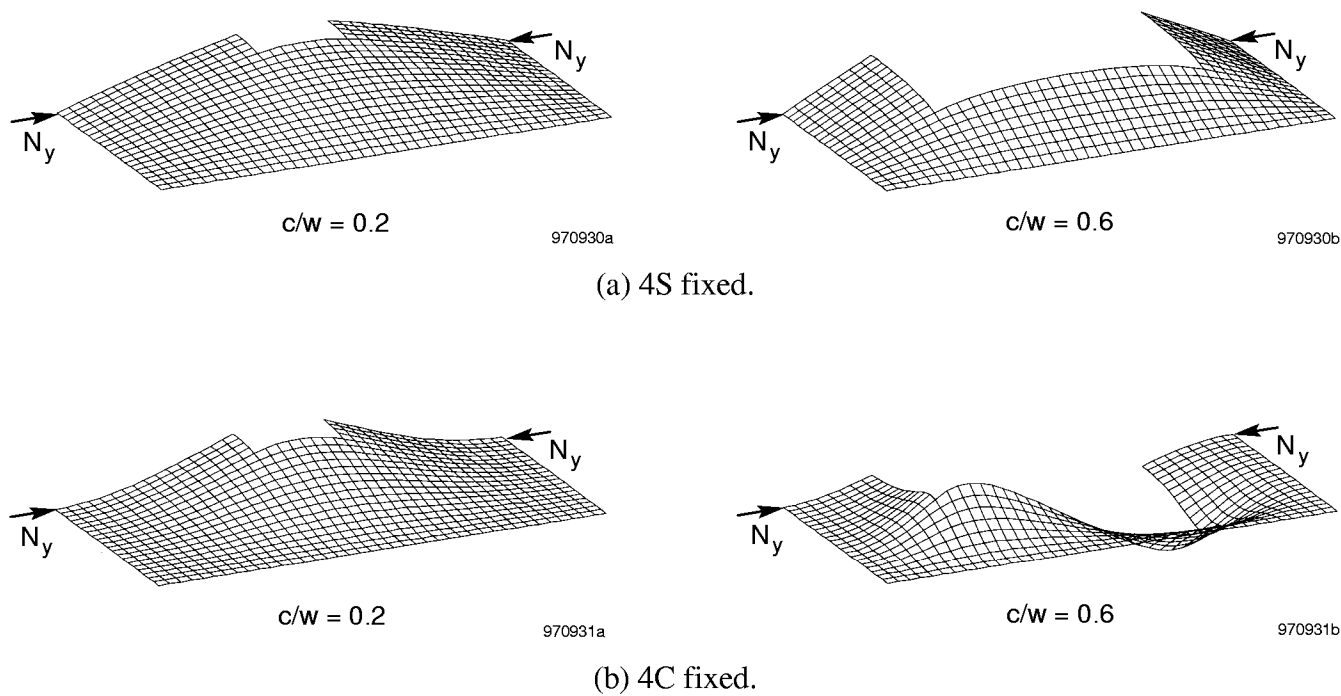


Figure 30. Buckled shapes of square plates with square holes under compression; $l/w = 1$; fixed edges.

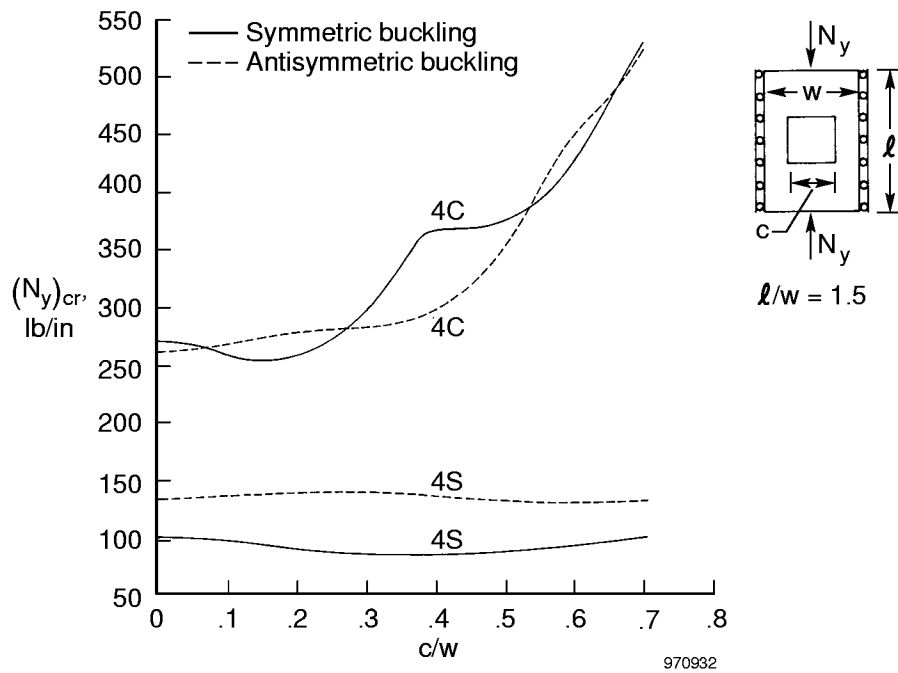


Figure 31. Compressive buckling loads as functions of hole size; square holes; fixed edges.

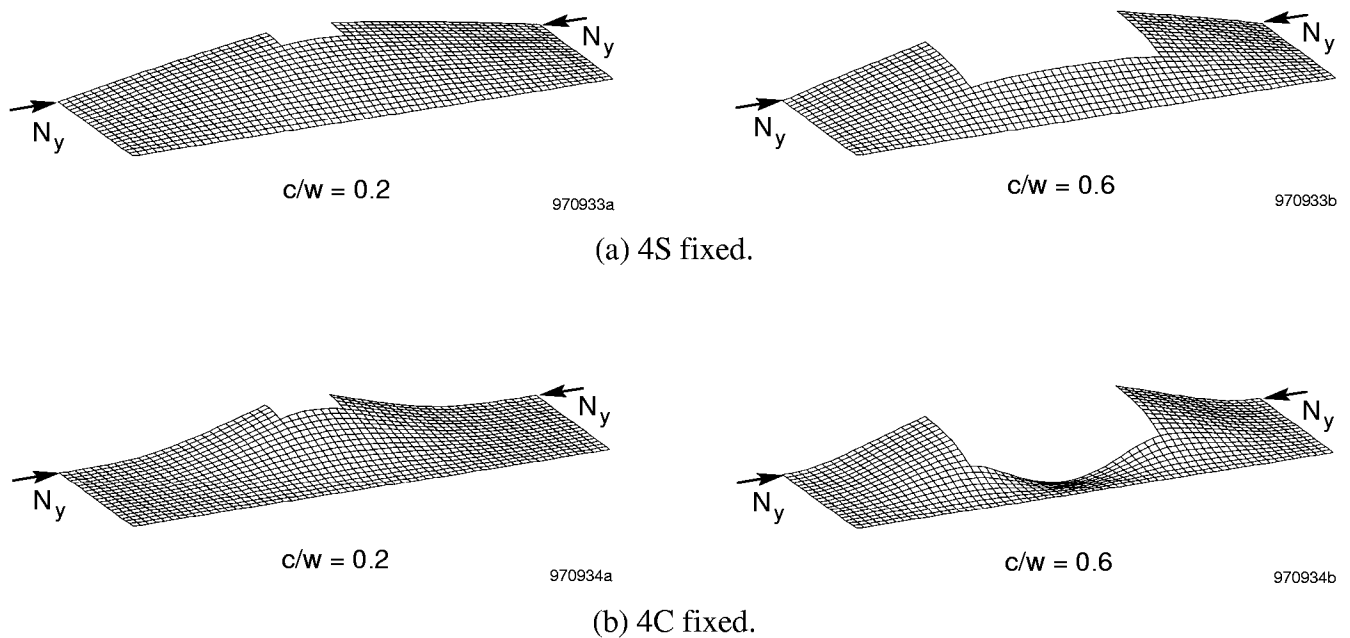


Figure 32. Buckled shapes of rectangular plates with square holes under compression; $l/w = 1.5$; fixed edges.

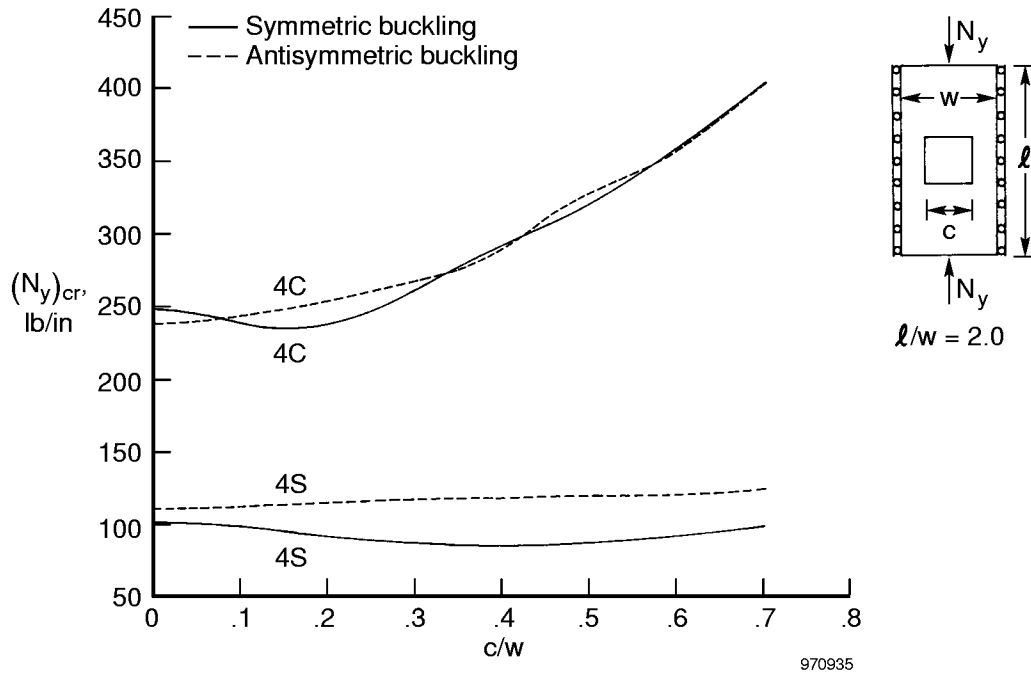


Figure 33. Compressive buckling loads as functions of hole size; square holes; fixed edges.

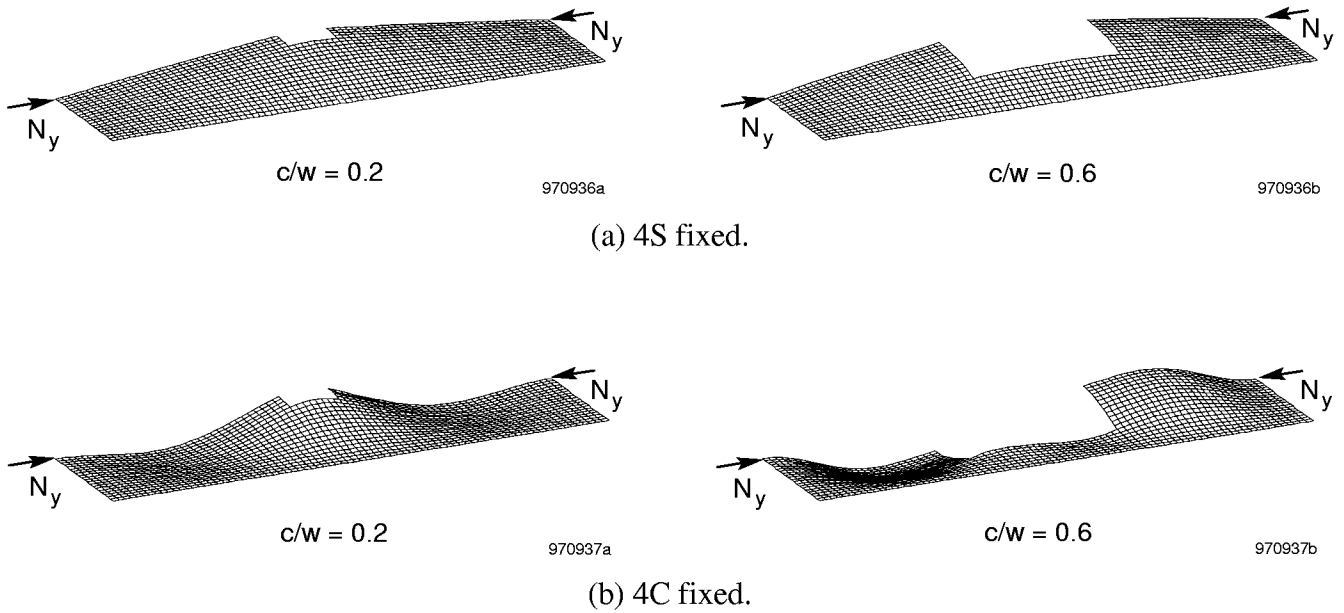


Figure 34. Buckled shapes of rectangular plates with square holes under compression; $l/w = 2$; fixed edges.

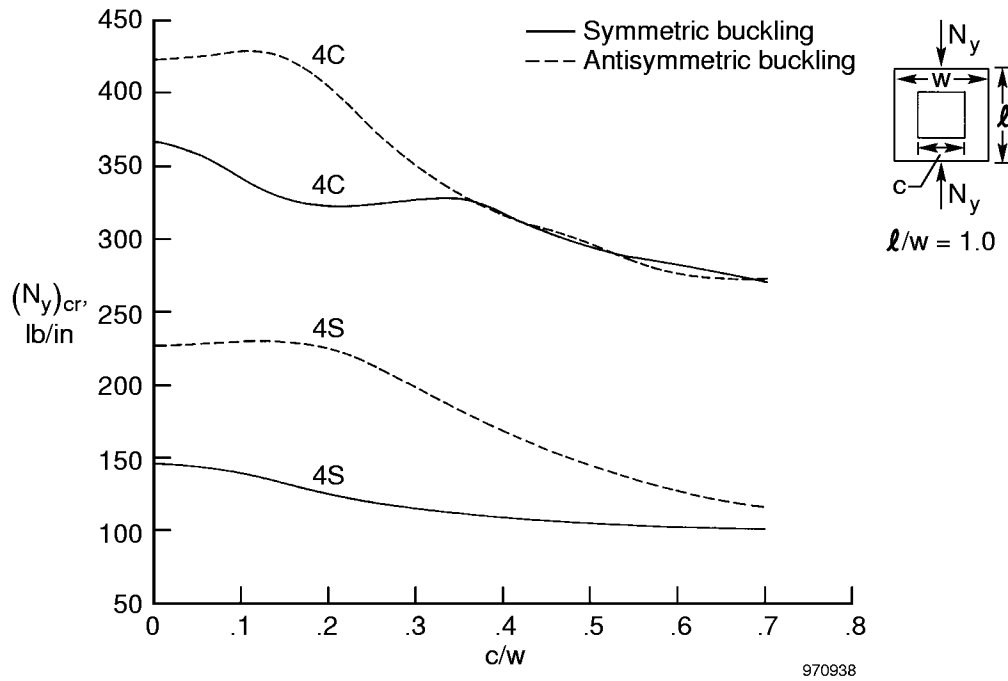


Figure 35. Compressive buckling loads as functions of hole size; square holes; free edges.

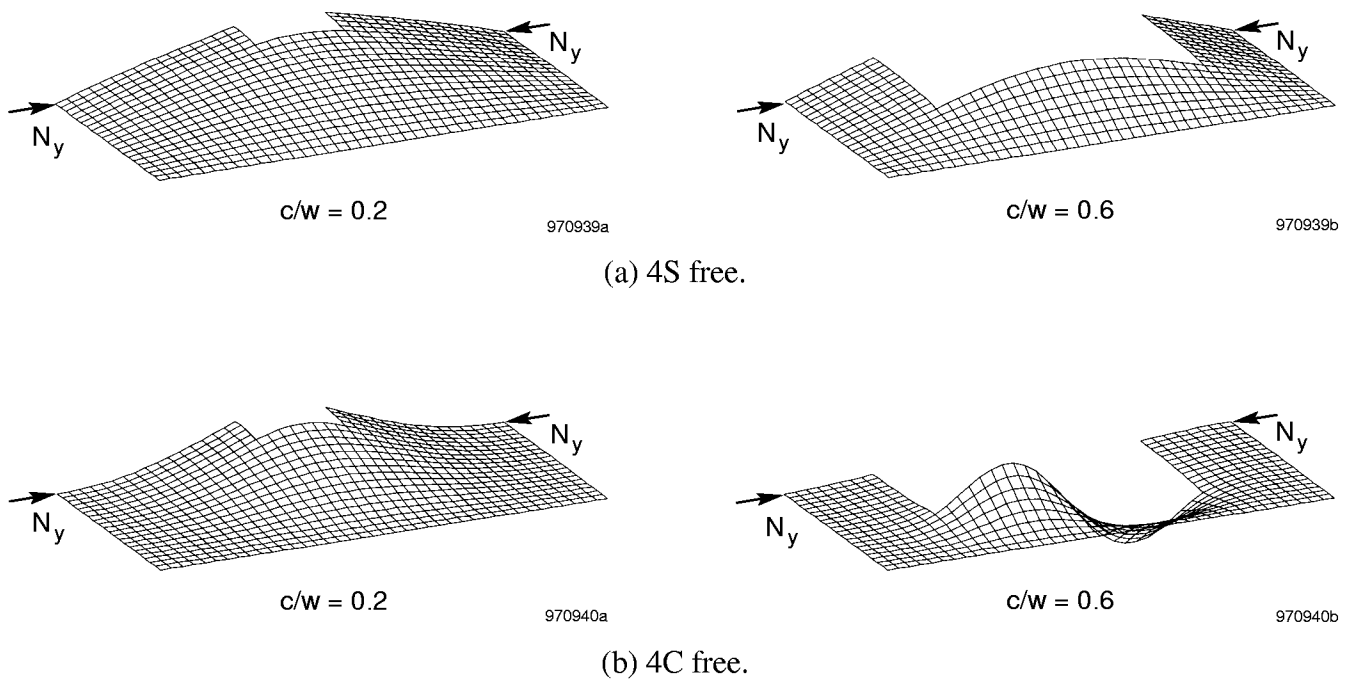


Figure 36. Buckled shapes of square plates with square holes under compression; $l/w = 1$; free edges.

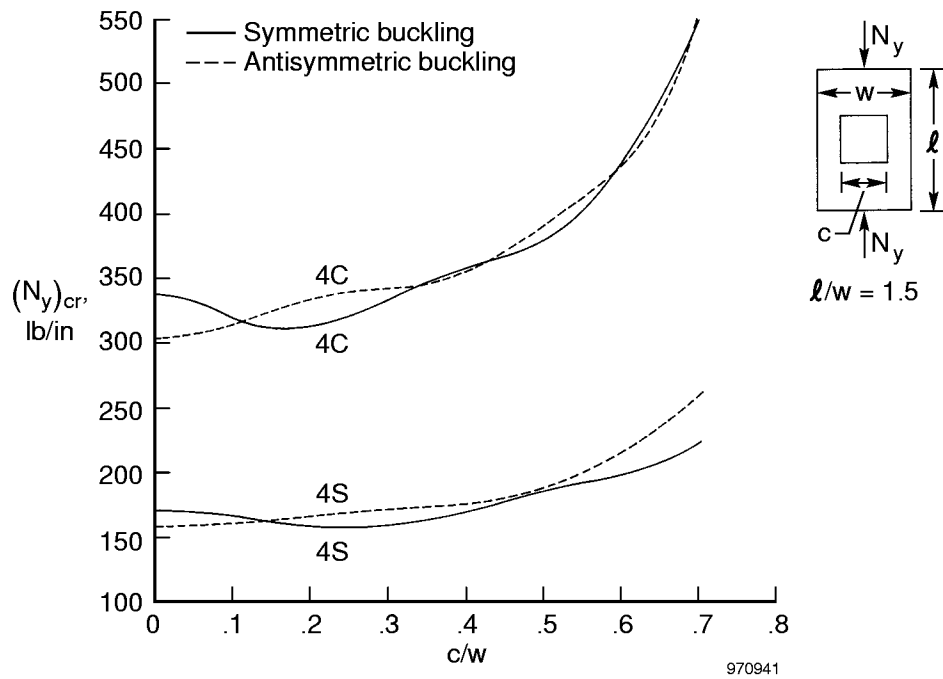


Figure 37. Compressive buckling loads as functions of hole size; square holes; free edges.

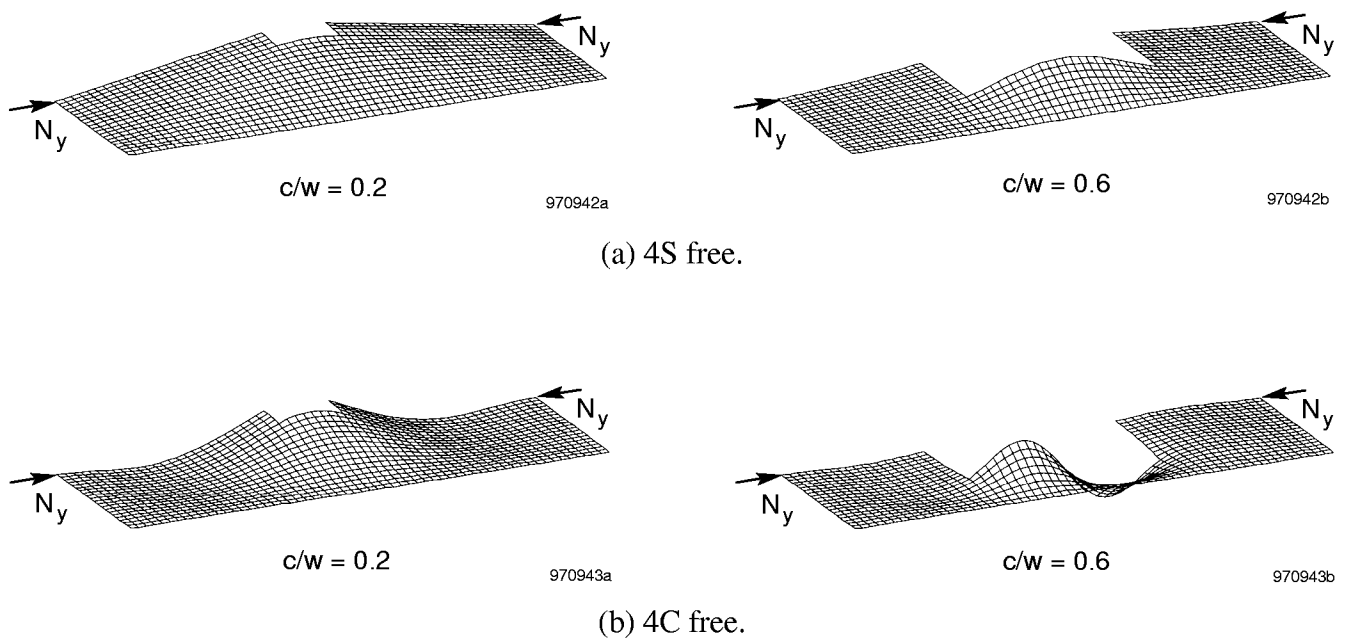


Figure 38. Buckled shapes of rectangular plates with square holes under compression; $l/w = 1.5$; free edges.

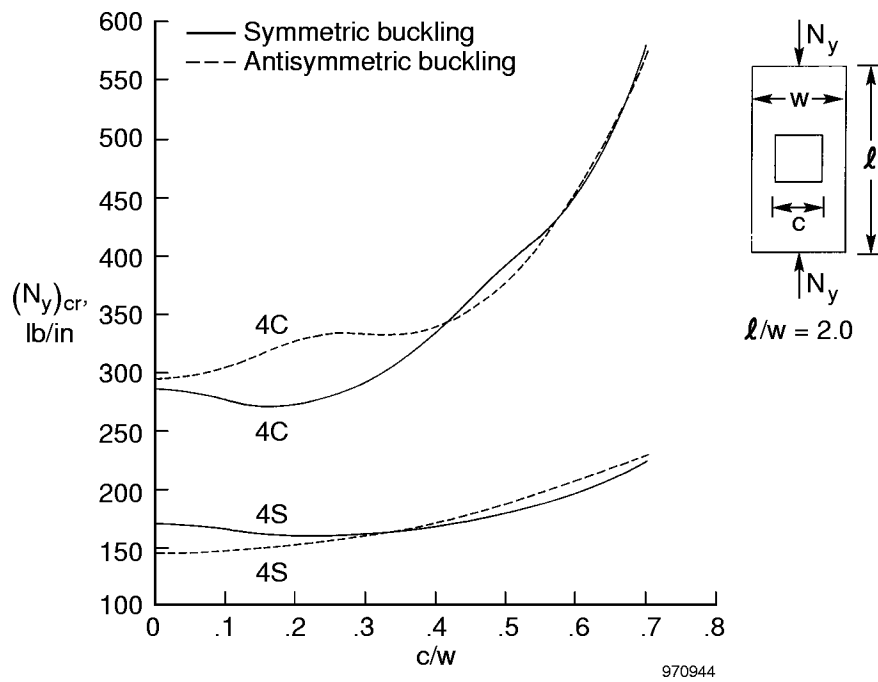


Figure 39. Compressive buckling loads as functions of hole size; square holes; free edges.

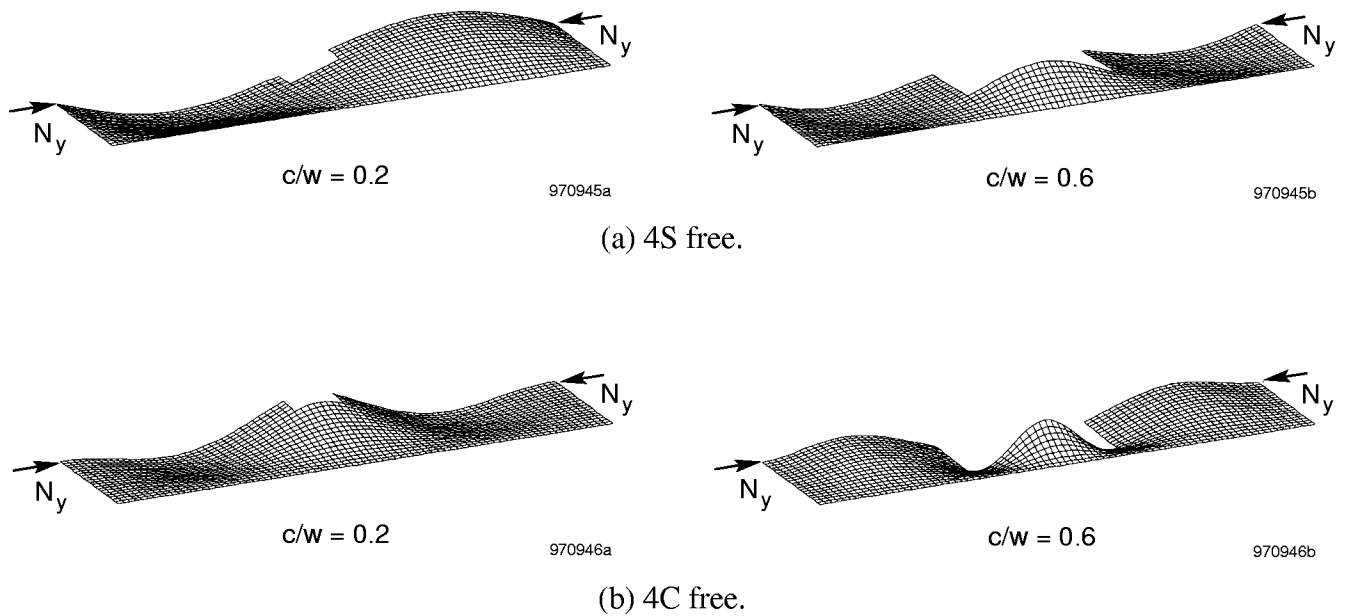


Figure 40. Buckled shapes of rectangular plates with square holes under compression; $l/w = 2$; free edges.

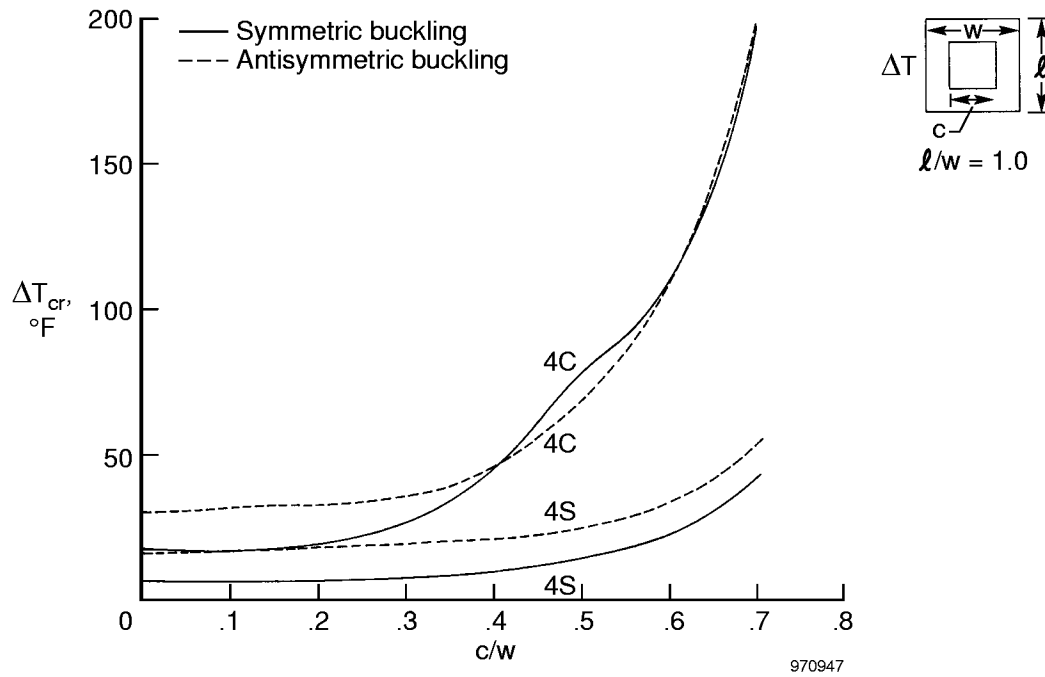
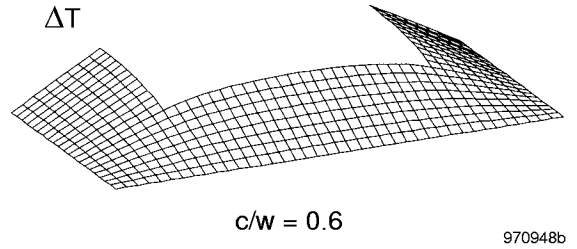
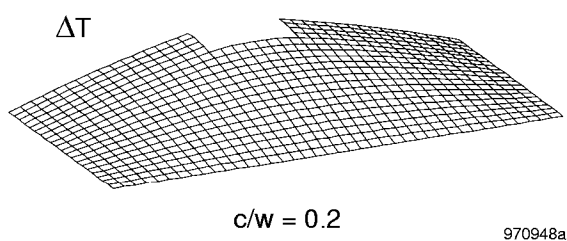
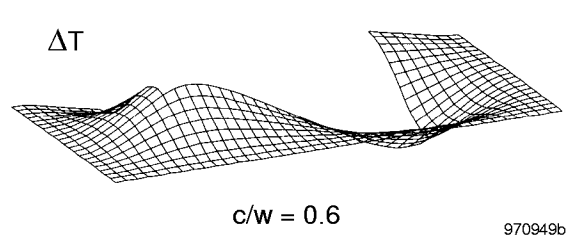
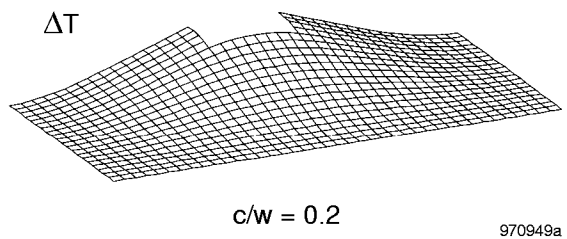


Figure 41. Buckling temperatures as functions of hole size; square holes.



(a) 4S fixed.



(b) 4C fixed.

Figure 42. Buckled shapes of uniformly heated square plates with square holes; $l/w = 1$.

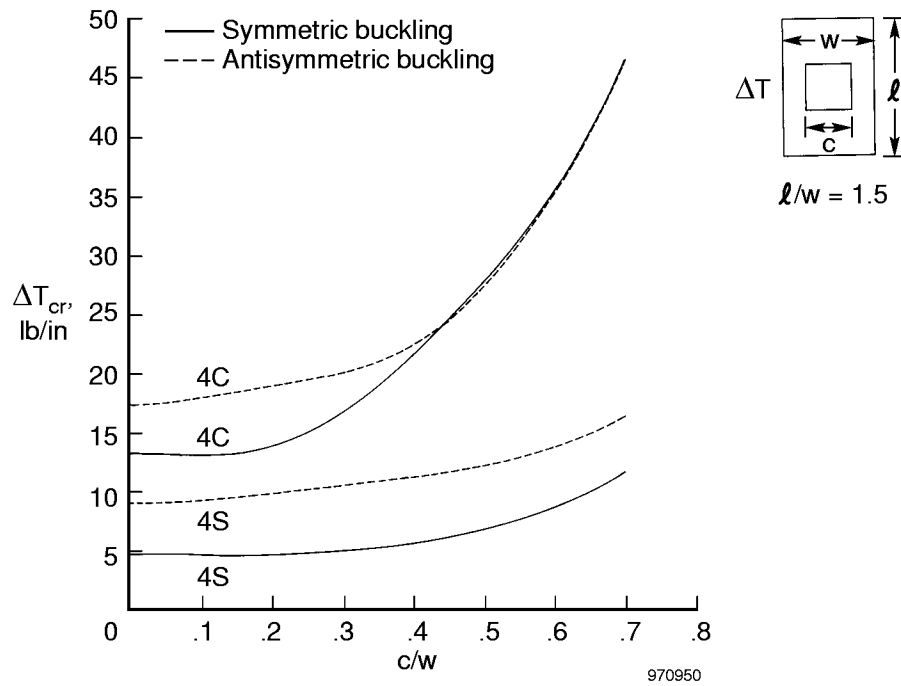


Figure 43. Buckling temperatures as functions of hole size; square holes.

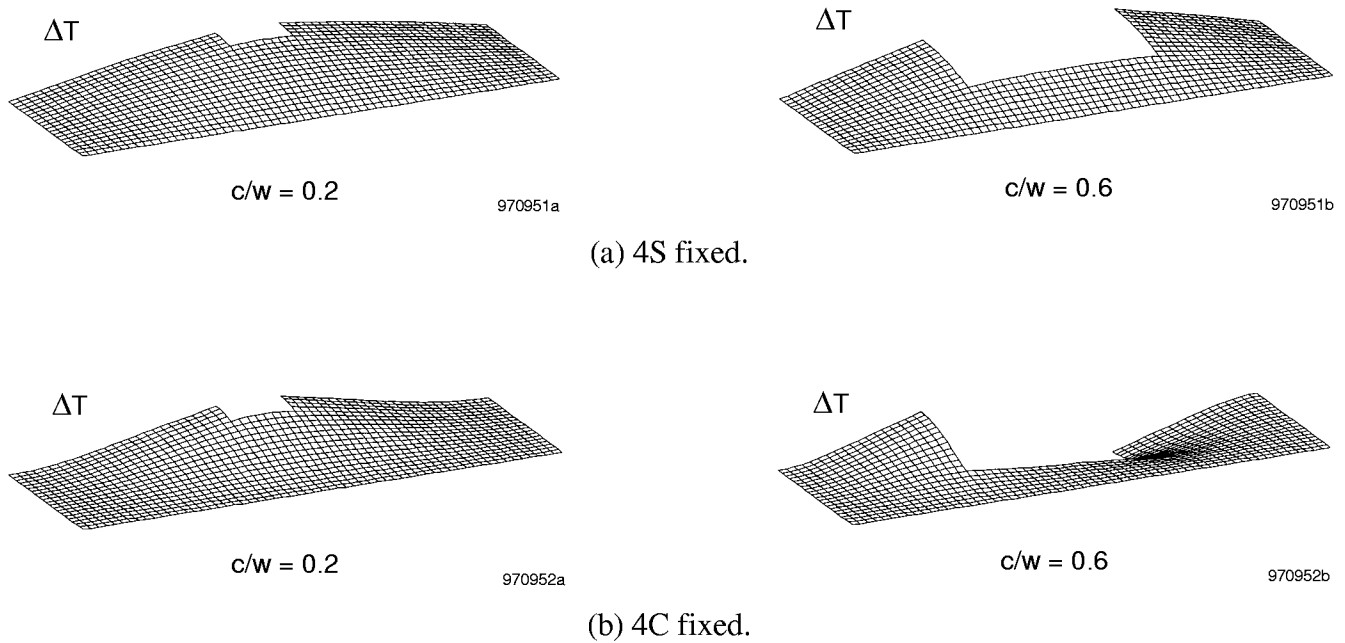


Figure 44. Buckled shapes of uniformly heated rectangular plates with square holes; $l/w = 1.5$.

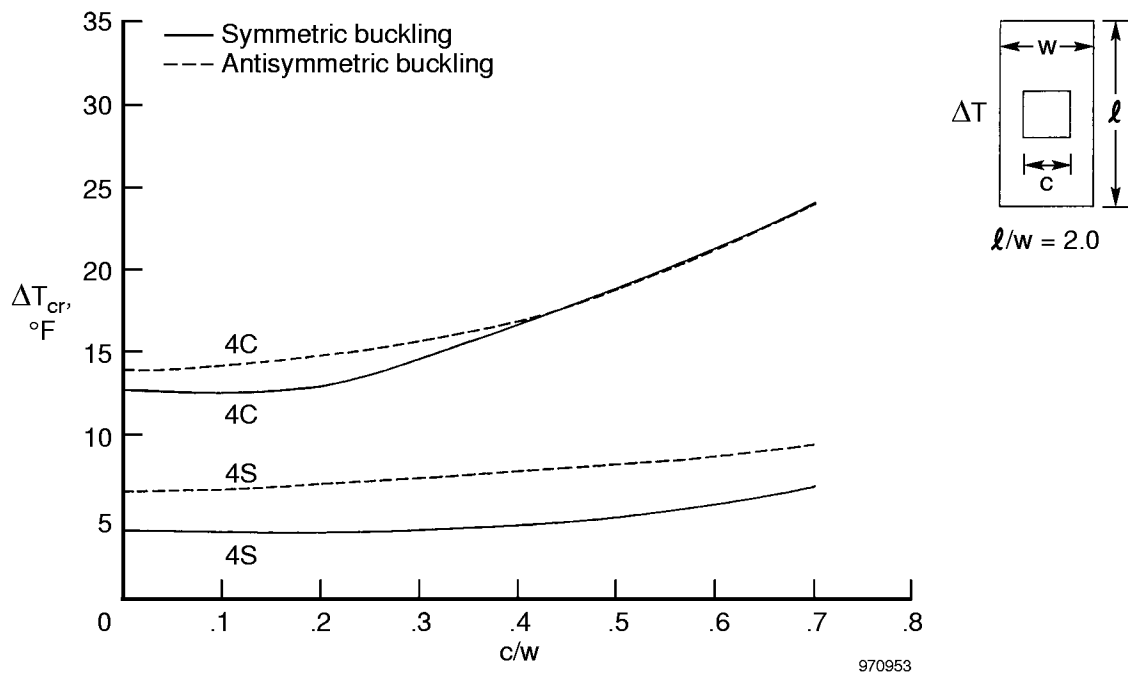


Figure 45. Buckling temperatures as functions of hole size; square holes.

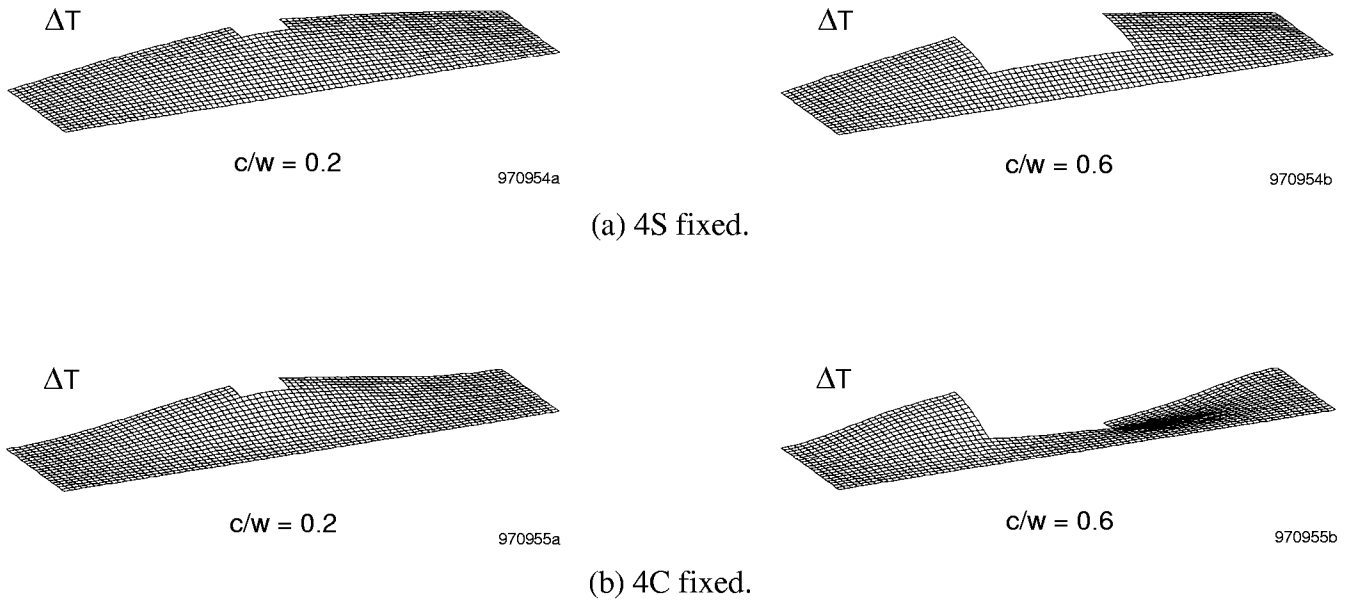


Figure 46. Buckled shapes of uniformly heated rectangular plates with square holes; $l/w = 2$.

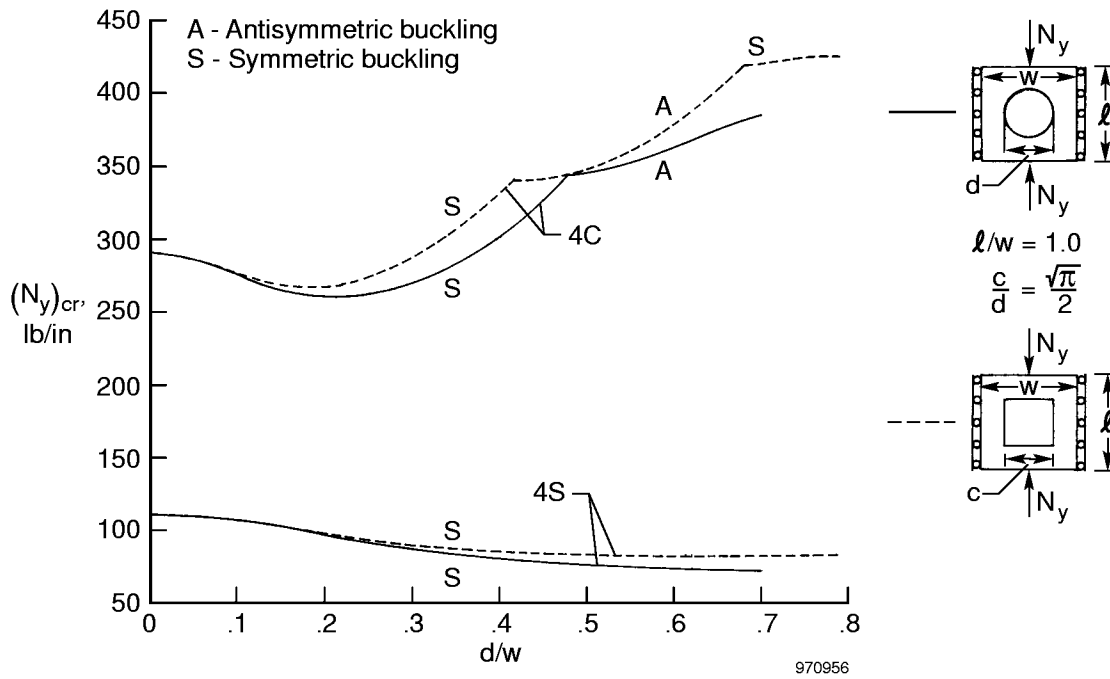


Figure 47. Comparison of compressive buckling strengths of square plates with different geometrical cutouts; fixed edges.

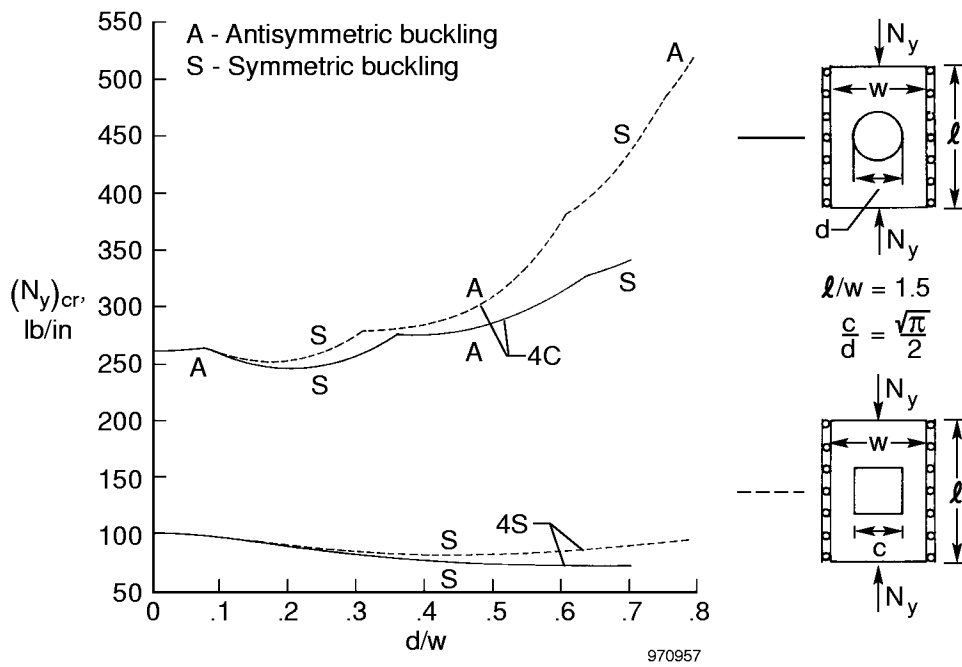


Figure 48. Comparison of compressive buckling strengths of rectangular plates with different geometrical cutouts; fixed edges.

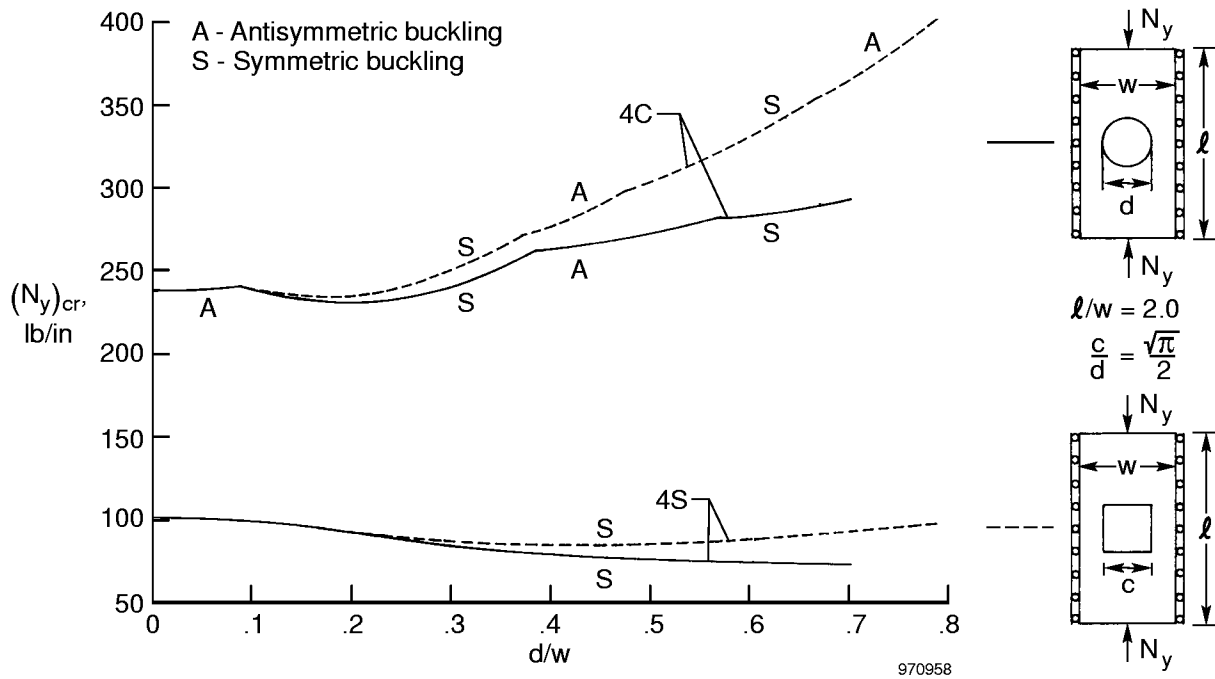


Figure 49. Comparison of compressive buckling strengths of rectangular plates with different geometrical cutouts; fixed edges.

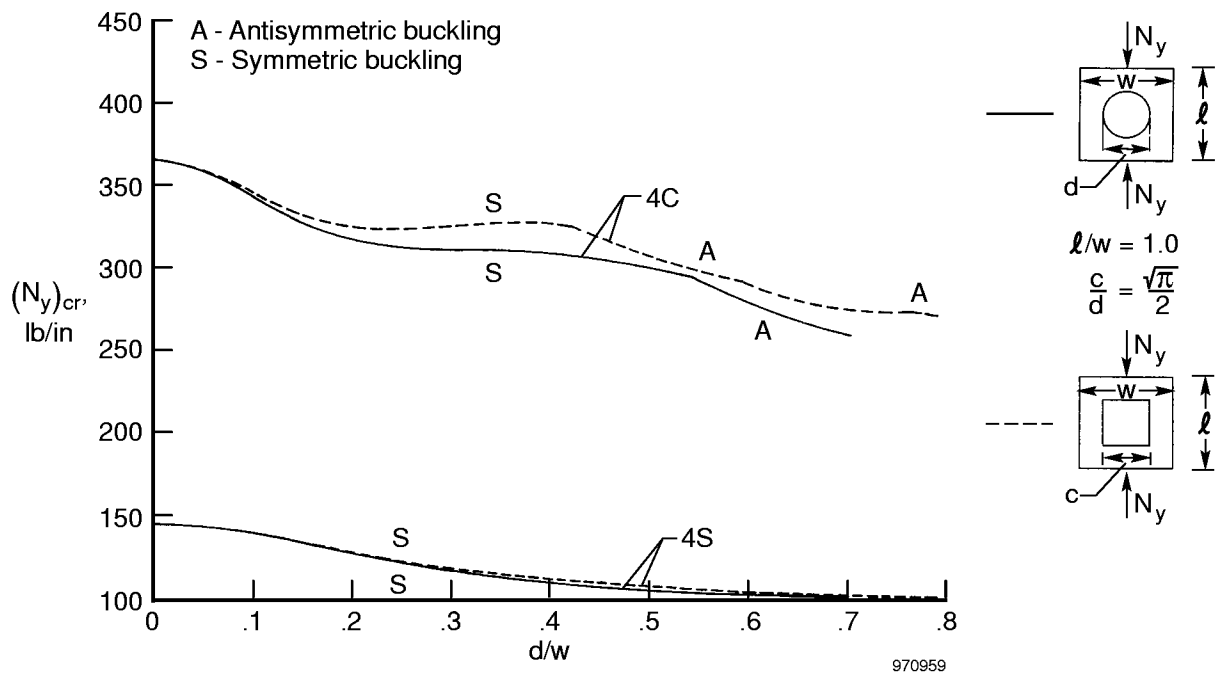


Figure 50. Comparison of compressive buckling strengths of square plates with different geometrical cutouts; free edges.

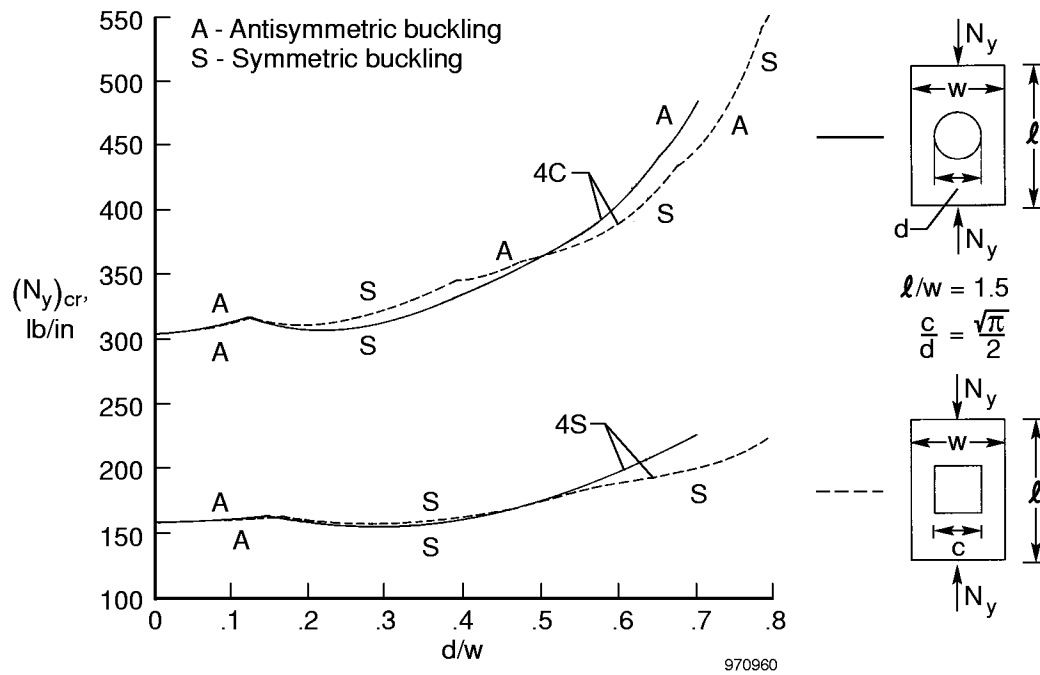


Figure 51. Comparison of compressive buckling strengths of rectangular plates with different geometrical cutouts; free edges.

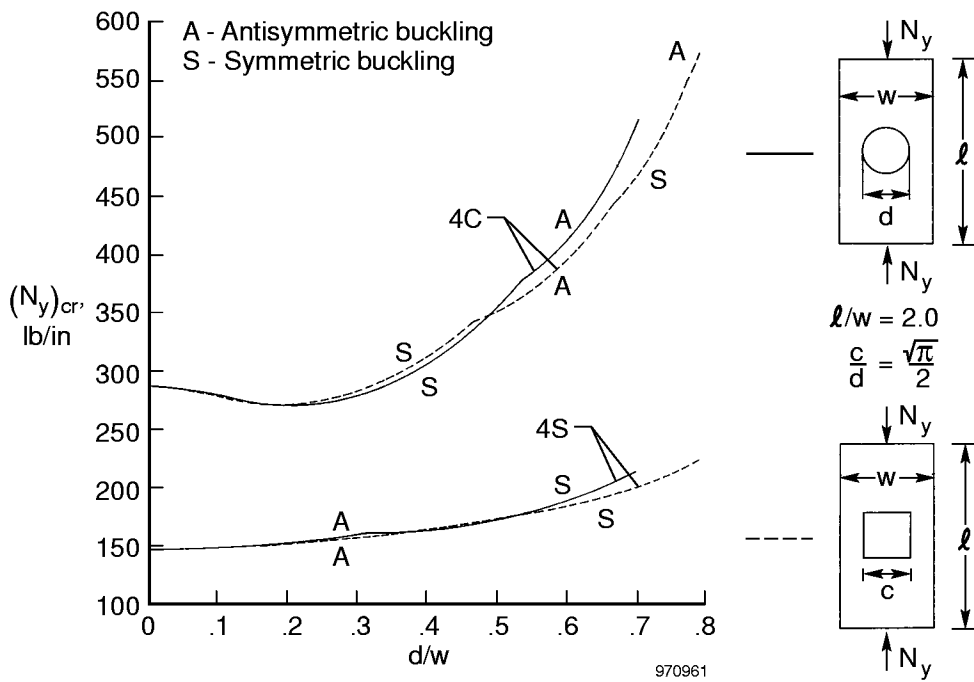


Figure 52. Comparison of compressive buckling strengths of rectangular plates with different geometrical cutouts; free edges.

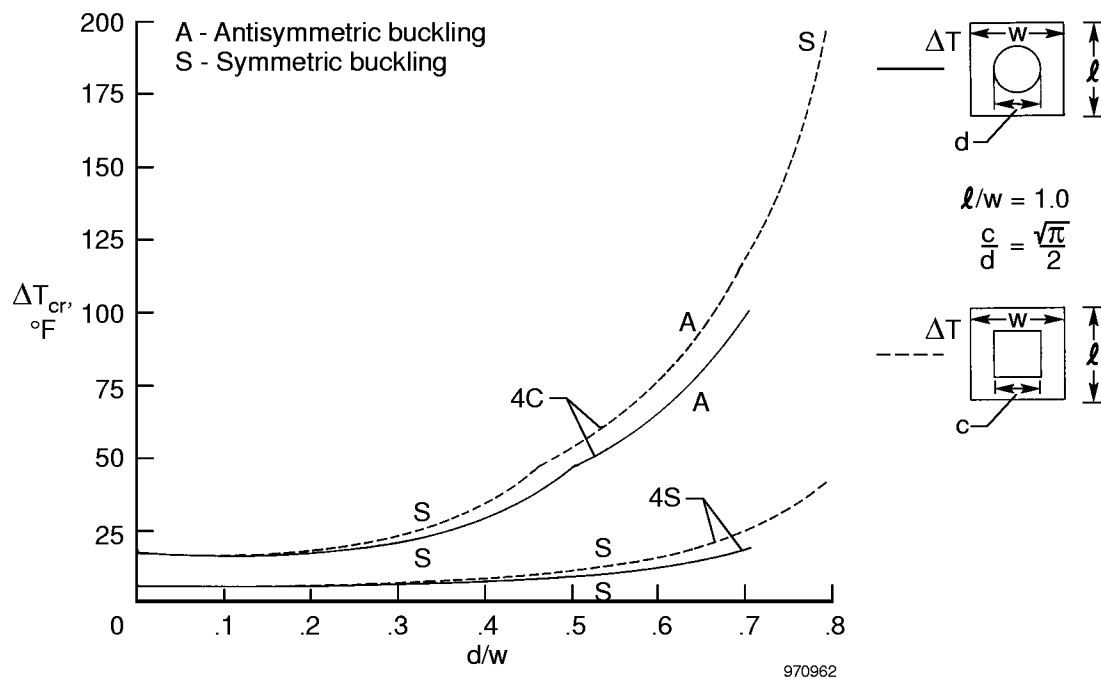


Figure 53. Comparison of thermal buckling strengths of square panels with different geometrical cutouts.

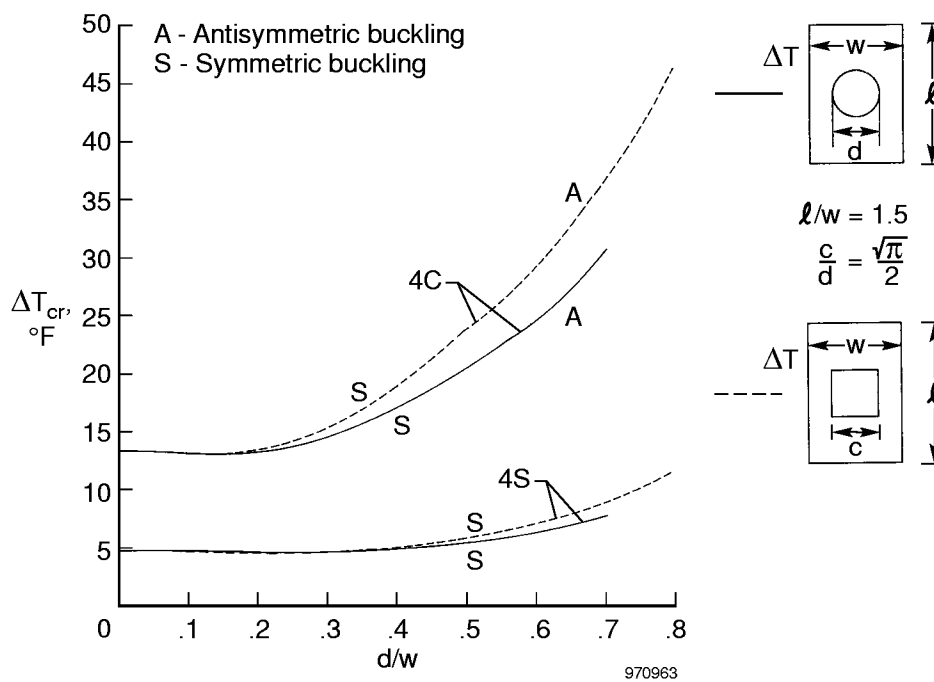


Figure 54. Comparison of thermal buckling strengths of rectangular panels with different geometrical cutouts.

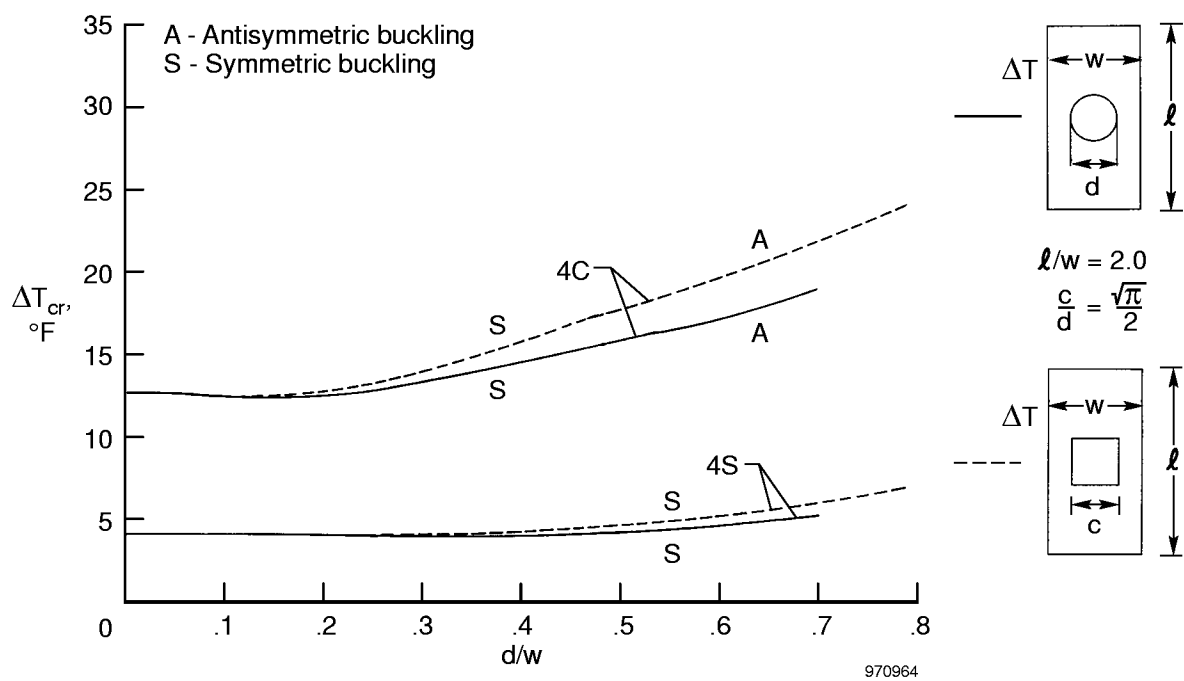


Figure 55. Comparison of thermal buckling strengths of rectangular panels with different geometrical cutouts.

REPORT DOCUMENTATION PAGE			Form Approved OMB No. 0704-0188	
Public reporting burden for this collection of information is estimated to average 1 hour per response, including the time for reviewing instructions, searching existing data sources, gathering and maintaining the data needed, and completing and reviewing the collection of information. Send comments regarding this burden estimate or any other aspect of this collection of information, including suggestions for reducing this burden, to Washington Headquarters Services, Directorate for Information Operations and Reports, 1215 Jefferson Davis Highway, Suite 1204, Arlington, VA 22202-4302, and to the Office of Management and Budget, Paperwork Reduction Project (0704-0188), Washington, DC 20503.				
1. AGENCY USE ONLY (Leave blank)		2. REPORT DATE March 1998		3. REPORT TYPE AND DATES COVERED Technical Memorandum
4. TITLE AND SUBTITLE Mechanical- and Thermal-Buckling Behavior of Rectangular Plates With Different Central Cutouts			5. FUNDING NUMBERS WU 522 32 34	
6. AUTHOR(S) William L. Ko				
7. PERFORMING ORGANIZATION NAME(S) AND ADDRESS(ES) NASA Dryden Flight Research Center P.O. Box 273 Edwards, California 93523-0273			8. PERFORMING ORGANIZATION REPORT NUMBER H-2206	
9. SPONSORING/MONITORING AGENCY NAME(S) AND ADDRESS(ES) National Aeronautics and Space Administration Washington, DC 20546-0001			10. SPONSORING/MONITORING AGENCY REPORT NUMBER NASA/TM-1998-206542	
11. SUPPLEMENTARY NOTES				
12a. DISTRIBUTION/AVAILABILITY STATEMENT Unclassified—Unlimited Subject Category 39			12b. DISTRIBUTION CODE	
13. ABSTRACT (Maximum 200 words) <p>Mechanical- and thermal-buckling analyses were performed on rectangular plates with central cutouts. The cutouts were either circular holes or square holes. The finite-element structural analysis method was used to study the effects of plate-support conditions, plate aspect ratio, hole geometry, and hole size on the mechanical- and thermal-buckling strengths of the perforated plates. By increasing the hole size, thermal-buckling strengths of the plates could be enhanced. The compressive-buckling strengths of the plates could also be increased considerably only under certain boundary conditions and aspect ratios. The plate-buckling mode can be symmetrical or antisymmetrical, depending on the plate boundary conditions, aspect ratio, and the hole size. For the same cutout areas (i.e., same plate weight density), the buckling strengths of the same-sized plates with square holes generally surpass those of the plates with circular holes over the range of hole sizes. The results and illustrations provide vital information for the efficient design of aerospace structural panels.</p>				
14. SUBJECT TERMS Buckling mode shapes, Mechanical buckling, Plates with circular holes, Plates with square holes, Thermal buckling			15. NUMBER OF PAGES 48	
			16. PRICE CODE A03	
17. SECURITY CLASSIFICATION OF REPORT Unclassified	18. SECURITY CLASSIFICATION OF THIS PAGE Unclassified	19. SECURITY CLASSIFICATION OF ABSTRACT Unclassified	20. LIMITATION OF ABSTRACT Unlimited	